

WIDE BINARIES FROM GAIA EDR3: PREFERENCE FOR GR OVER MOND ?

C. PITTORDIS AND W. SUTHERLAND

The School of Physical and Chemical Sciences, Queen Mary University of London, Mile End Road, London E1 4NS, UK.

(Dated: Accepted by Open Journal of Astrophysics, 31 Jan 2023; original submission 13 July 2022)

Version February 2, 2023

ABSTRACT

Several recent studies have shown that velocity differences of very wide binary stars, measured to high precision with GAIA, can potentially provide an interesting test for modified-gravity theories which attempt to emulate dark matter. These systems should be entirely Newtonian according to standard dark-matter theories, while the predictions for MOND-like theories are distinctly different, if the various observational issues can be overcome. Here we provide an updated version of our 2019 study using the recent GAIA EDR3 data release: we select a large sample of 73 159 candidate wide binary stars with distance ≤ 300 parsec and magnitudes $G < 17$ from GAIA EDR3, and estimate component masses using a main-sequence mass-luminosity relation. We then examine the frequency distribution of pairwise relative projected velocity (relative to circular-orbit value) as a function of projected separation, compared to simulations; as before, these distributions show a clear peak at a value close to Newtonian expectations, along with a long ‘tail’ which extends to much larger velocity ratios and may well be caused by hierarchical triple systems with an unresolved or unseen third star. We then fit these observed distributions with a simulated mixture of binary, triple and flyby populations, for GR or MOND orbits, and find that standard gravity is somewhat preferred over one specific implementation of MOND; though we have not yet explored the full parameter space of triple population models and MOND versions. Improved data from future GAIA releases, and followup of a subset of systems to better characterise the triple population, should allow wide binaries to become a decisive test of GR vs MOND in the future.

1. INTRODUCTION

Einstein’s theory of General Relativity (GR) is perceived to be the best description of gravity on all scales. GR has been very well tested in the Solar System, but requires exotic dark matter (DM) to explain larger structures such as galaxies, clusters, and the cosmic microwave background (CMB) within the GR-based Λ CDM cosmological model (Planck Collaboration XIII 2016). At present time, there is no decisive direct detection of DM (e.g. Akerib et al. (2016)); though there are many lines of indirect evidence, primarily via flat rotation curves (RCs) of galaxies, gravitational lensing, galaxy clustering and the CMB. Moreover, the Λ CDM picture leads to several small-scale discrepancies between numerical simulations based on DM and observations on sub-galactic scales (Kroupa 2015; Bullock & Boylan-Kolchin 2017), perhaps most seriously with the Local Group satellite planes (Pawlowski et al. 2014).

This leaves room for modified gravity (MG) theories such as the notable Modified Newtonian Dynamics (MOND) (Milgrom 1983) as an alternative to GR. MOND (reviewed in Famaey & McGaugh 2012) attempts to explain the observations usually attributed to dark matter by a suitable modification of standard GR. The original MOND formulation was non-relativistic and really a fitting function rather than a realistic theory; it has later been incorporated into relativistic theories following from the well-known Tensor-Vector-Scalar (TeVeS) theory proposed by Bekenstein (2004). There are various versions of MG, but figure 10 from Famaey & McGaugh (2012) indicates that the most promising should

involve a departure from Newtonian gravity at accelerations below some threshold a_0 , as occurs in MOND. The current situation of Λ CDM vs MOND remains contentious, with many successes for Λ CDM on large scales but some anomalies on galactic and sub-galactic scales; while MOND appears mostly successful on galactic scales but has no clear-cut predictions for cosmology.

As noted in Pittordis & Sutherland (2019, hereafter PS19), a clear convincing direct detection of dark matter in underground experiments would be the most decisive scenario, but the converse is not true: null results from dark matter detectors can never rule out the paradigm, because the DM interaction cross-section might simply be too small for any practical experiment (or, the cross-section could be weak-like but the DM particle masses could be very large $\sim 10^9$ GeV, implying a local number density far below the value for conventional TeV-scale WIMPs). Therefore, in the absence of a DM direct detection, new tests which can discriminate between DM and modified gravity from direct tests of gravity at the relevant very low accelerations are highly desirable.

A promising test of MG is via wide binary (WB) stellar systems in the Solar neighbourhood (within ≈ 250 pc, Hernandez et al. 2012b). WBs are isolated stellar pairs with separations $\gtrsim 7$ kAU in order to have orbital accelerations $\lesssim a_0 = 1.2 \times 10^{-10}$ m/s². The small size of WBs means no significant amount of DM should be distributed within them, so Keplerian dynamics should apply in GR+DM models. In a MOND context, local WBs must feel the Galactic external field which is slightly larger than a_0 , and the external field effect results in WB orbital velocities exceeding the Newtonian prediction by $\sim 20\%$ (Banik & Zhao 2018) for an interpolating function

E-mail: cp.pittordis@gmail.com
E-mail: w.j.sutherland@qmul.ac.uk

consistent with galaxy RCs (McGaugh et al. 2016). This excess $\approx 20\%$ remains approximately constant at larger WB separations, although WB tests are more prone to observational caveats at larger separations. Studies of WBs in general have been explored by e.g. Weinberg et al. (1987), Close et al. (1990), Yoo et al. (2004), Lépine & Bongiorno (2007), Kouwenhoven et al. (2010), Jiang & Tremaine (2010), Dhital et al. (2013), Coronado et al. (2018), and others.

Previous work concerning tests of MOND-like gravity has been done by Hernandez et al. (2012b), Hernandez et al. (2012a), Hernandez et al. (2014), Matvienko & Orlov (2015), Scarpa et al. (2017) and Hernandez (2019); these typically give hints of deviations in the direction expected from MOND-like gravity, though due to the limited precision of the pre-GAIA data used, these hints were not decisive. If modelled appropriately, WBs can provide a very ‘clean’ model-independent test of gravity in the extremely weak-field regime relevant to galactic outskirts and large scale structure. Note that the orbital periods of WBs are \sim Myr, so accelerations are undetectable and full orbit modelling is not possible, thus each single binary is strongly under-constrained; however the statistical distribution of relative velocities is readily predicted from simulations assuming random phases and inclinations, so a large sample of thousands of WBs can provide a sensitive test.

In our first paper in this series (Pittordis & Sutherland 2018, hereafter PS18), we used simulations to explore the prospects for this wide-binary test, in anticipation of the much improved data from the GAIA spacecraft (Gaia Collaboration 2016); PS18 used simulated wide-binary orbits for a variety of acceleration laws, including Newtonian and various MOND models both with and without an external field effect (hereafter ExFE); the general conclusion was that GAIA data provides promising prospects for such a test, since MOND-like models without an ExFE should produce large and obvious deviations towards larger velocity differences. In MOND-like models with the ExFE included, as theoretically preferred, the local Galactic acceleration field substantially suppresses MOND-like effects, but does not eliminate them. These models with ExFE give predicted relative velocities much closer to Newtonian, but do still show subtle deviations, most notably a significantly larger fraction of binaries with pairwise velocities in the range $(1.1 - 1.5) \times v_C(r_p)$, where $v_C(r_p)$ is the Newtonian circular velocity at projected separation r_p . Here we recall two of the main conclusions from PS18: MOND-like theories can allow bound binaries with relative velocities above the Newtonian ceiling, $v_{3D}/v_C(r_p) > \sqrt{2}$, (where v_{3D} is the 3-D pairwise relative velocity); but with the ExFE included the fraction of such systems is predicted to be very small, typically 1 percent or less; so simply counting such systems is unlikely to be a practical test due to possible contamination, observational errors, and small-number statistics. However, the upper percentiles of this velocity ratio, or similarly the fraction of binaries with velocity ratio between $\sim 1.1 - 1.5$ are more promising statistics. In particular, the upper tail (top ~ 10 percent) of the binary velocity distribution is only weakly sensitive to the rather uncertain eccentricity distribution, but is strongly sensitive to modified gravity.

The second main conclusion from PS18 was that, in

MOND theories including the ExFE, there is an optimal window of binary projected separations, $5 \lesssim r_p \lesssim 20$ kAU, for practical application of the test. Even wider separations are not favoured in practice because the inclusion of the ExFE causes the MOND-like effects to almost saturate at a fixed percentage at $r_p \gtrsim 10$ kAU, while several observational issues become proportionally worse at even wider separations $\gtrsim 20$ kAU.

After the release of GAIA Data Release 2, we explored an observational application of the test with that dataset (Pittordis & Sutherland 2019, hereafter PS19) (see also Hernandez (2019) and Hernandez et al. (2022) for related studies with GAIA data). Since the 3D separation r is not a practical observable (since the line-of-sight separation is typically well below the precision of distance measurements, even for GAIA) we have to replace it with projected separation r_p as a proxy, which shifts the ratios to lower values depending on viewing angles; but this effect can be readily included in simulations. The main conclusions of PS19 were that there is a sufficient population of bound binaries to carry out the test in future, but also that there exists a “tail” of pairs with large velocity differences, too numerous to explain by random alignments. This may be accounted for by common-origin unbound pairs (as modelled in PS19), or perhaps a more likely explanation by Clarke (2020) is hierarchical triples with an unresolved or faint third star in a closer orbit, which boosts the observed velocity difference between the two visible stars.

In this paper we provide an updated version of PS19, using the recent GAIA Early Data Release 3 (Gaia Collaboration 2020a,b) to provide a $\sim 3\times$ larger sample of candidate WBs, with more precise proper motions. We also update our modelling here to fit the observed distributions with a mixture of binary, triple and flyby systems, using both Newtonian and MOND gravity laws and various eccentricity distributions.

The plan of this paper is as follows: in Section 2 we describe the methods for selecting candidate wide-binaries from the GAIA Early Data Release 3 (hereafter, EDR3) data and cleaning the sample; we then compare to the earlier sample from Pittordis & Sutherland (2019), and the EDR3 sample from El-Badry et al. (2021). In Section 3 we discuss various simulations of the velocity-ratio distributions for Newtonian and the realistic MOND-like binary orbits (with ExFE) from (Banik & Zhao 2018, hereafter BZ18); and we also simulate triple star systems, which appear to provide a reasonable fit to the high-velocity tail of the distribution, $v_p/v_C(r_p) \geq \sqrt{2}$, and unbound flyby systems. In Section 4 we fit the observed distributions with a mixture of simulated binary, triple and flyby model populations, for both GR and MOND cases; and we summarise our conclusions in Section 5.

2. GAIA EDR3 AND SAMPLE SELECTION

2.1. Preliminary selection

Our starting point is the public GAIA Early Data Release 3 dataset (EDR3), (Gaia Collaboration 2020a,b) released on 2020 December 3. We initially select all stars with measured parallax $\omega > \frac{10}{3}$ mas (i.e. estimated distance < 300 pc) with a GAIA broadband magnitude $G < 17$, and cutting out the Galactic plane with absolute latitude $|b| \leq 15$ deg yielding a preliminary EDR3 sam-

ple of 2,101,920 stars (hereafter PEDR3). (Data quality cuts are applied at a later stage, in order that these may be adjusted post-selection). These criteria are expanded from 200 pc and $G < 16$ used by PS19 from Gaia Data Release 2 (hereafter, DR2), since the improved data quality in EDR3 allows an expanded volume while giving slightly smaller transverse velocity errors. The parallax and magnitude cuts above are chosen to provide a large enough volume to contain a usefully large statistical sample of wide binaries; while the moderate distance limit and relatively bright magnitude limit ensures that GAIA provides high precision on distances and transverse velocities.

We then used the same search method as described in section 2 from PS19 to search this nearby-star sample for pairs of stars with projected separation ≤ 50 kAU (calculated at the mean distance of each candidate pair), difference in parallax distances of both stars $|d_1 - d_2| \leq 8.0$ pc, and distances also consistent with each other within $4\times$ the combined uncertainty e.g., $|d_1 - d_2| \leq 4\sigma_d$, and projected velocity difference $\Delta v_p \leq 3$ km s $^{-1}$ as inferred from the difference in proper motions; here, the projected velocity difference is computed assuming *both* stars in each candidate pair are actually at the mean of the two estimated distances.

We note here that this common-distance assumption is important: if the relative velocities are calculated using individual parallax distances, then an example random 1 percent difference in parallax for a system with transverse velocity 40 km s $^{-1}$ scales to a 0.4 km s $^{-1}$ transverse velocity difference, which is similar to or larger than the orbital velocities of interest below. However, since we are almost entirely interested in the velocity *difference* within a binary, the common-distance assumption leads to an error in estimated relative velocity proportional to the unknown *true* fractional distance difference, $(d_1 - d_2)/d$ (see also Shaya & Olling (2011), and Section 2.4 of PS18 for related perspective effects). For true binaries with random orientation we expect $|d_1 - d_2| \leq r_p$ for 71 percent of systems, and $\leq 2r_p$ for 90 percent. Then for a typical binary (see below) with $r_p \sim 10$ kAU and $d \sim 180$ pc we have $r_p/d \sim 2.7 \times 10^{-4}$; this is much smaller than the fractional uncertainty of the parallaxes, so choosing the common-distance assumption yields a much more precise estimate of the relative velocity for *genuine* binaries.

This search results in a first-cut sample of 92,677 candidate EDR3 wide binaries (hereafter WB-EDR3); this sample is then pruned with additional cuts as described in the following subsections. The sky distribution of these candidates is shown in Figure 1 (left panel).

2.2. Triple and higher systems

To reject the majority of “moving groups” or similar, we searched our WB-EDR3 sample for any star in common between two or more candidate binaries; if so, both or all those binaries were rejected, reducing the WB-EDR3 sample to 83,884 candidate binaries with no star common to more than one candidate binary.

2.3. Sky cuts

Inspection of the WB-EDR3 sample showed a roughly uniform distribution across the sky, with some enhancement near around some well-known open clusters, i.e. the

TABLE 1
LIST OF COORDINATES FOR EXCLUDED REGIONS AROUND OPEN CLUSTERS.

Cluster	RA limits (deg)	Dec limits (deg)
Blanco 1	(0, 2)	(-31, -29)
Pleiades	(54, 59)	(+22, +27)
Praesepe	(129, 131)	(+18, +22)
Upper Sco	(238, 248)	(-29, -19)

Pleiades, Praesepe, Upper Sco, and the Blanco 1 open cluster. Similar to PS19, we applied sky cuts to eliminate regions around the above clusters; the details of the exclusion regions are listed in Table 1. These sky cuts reduce the sample to 83,100 candidate binaries.

2.4. Removing faint companions

Similar to the methods of PS19, we also searched for additional co-moving companion stars to a fainter limit: we selected a “faint star” sample of GAIA stars with $G < 20$ and a measured parallax $\omega > \frac{10}{3}$ mas (i.e. estimated distance < 300 pc); for each star in each candidate binary, we then searched for faint-star companions with the following criteria:

1. Parallax consistent with the main star at 4σ .
2. Angular separation less than $2/3$ of the main-binary separation (since hierarchical triples are expected to be unstable for inner-orbit separation above $\sim 0.4\times$ the outer separation); and angular separation above 0.5 arcsec to avoid barely-resolved companions.
3. Measured projected velocity difference from the main star ≤ 5 km s $^{-1}$.

If any such “third star” was found, (in 698 cases), we rejected the candidate binary since a hierarchical triple will generally boost the projected velocity difference of the wide pair; this left a de-tripled sample of 82,402 candidate binaries from the WB-EDR3 sample.

Clearly, the third-star search above will not reject third stars which are either very faint or unresolved from one of our binary members; this will need to be considered for possible follow-up observations later. We consider the effects of contamination from undetected triple systems later in section 3.2, showing this may be the dominant source of contamination.

2.5. Data quality cuts on wide binary candidates

We applied data-quality cuts to the WB-EDR3 sample based on the GAIA parameters, as Arenou et al. (2018) Equation 1 as follows:

$$\begin{aligned}
 \chi^2 &\equiv \text{astrometric_chi2_al} \\
 \nu &\equiv \text{astrometric_n_good_obs_al} - 5 \\
 u &\equiv \sqrt{\chi^2/\nu} \\
 u &\leq 1.2 \times \max(1, \exp[-0.2(G - 19.5)]) \quad (1)
 \end{aligned}$$

We rejected candidate pairs from the WB-EDR3 sample, where at least one star did not satisfy Eq. 1; this rejected 9,243 candidate pairs, leaving a cleaned sample of 73,159 candidate wide binaries, hereafter labelled CWB-EDR3: this is the main sample used for analysis below.

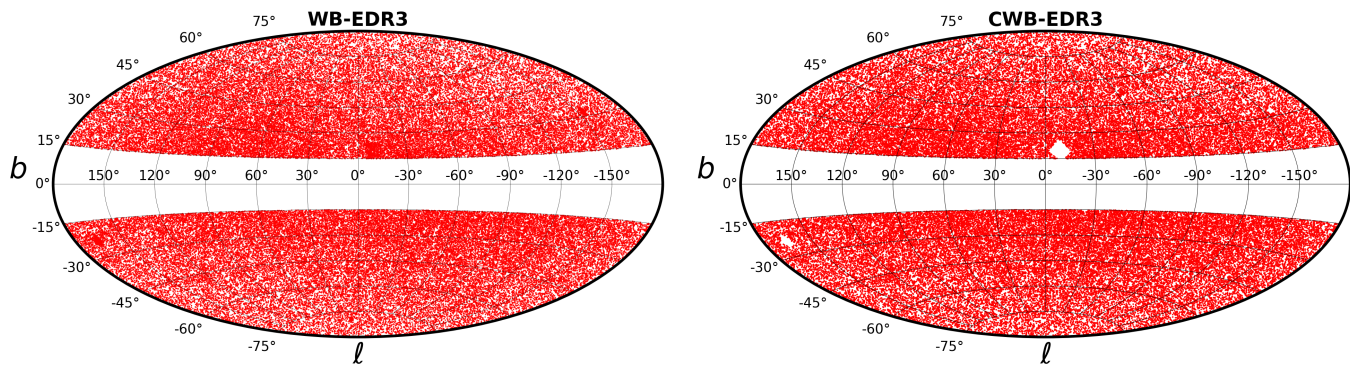


FIG. 1.— The sky distribution in Galactic coordinates for candidate binaries in EDR3: the left panel shows the initial set of candidate binaries WB-EDR3, the right panel is the cleaned sample CWB-EDR3 after applying all cuts in Section 2. Note that the holes from limited sky coverage in PS19 no longer appear with the improved coverage of EDR3.

2.6. Results and scaled velocities

For the surviving 73,159 candidate binaries, we show a plot of projected velocity difference vs projected separation in Figure 2; this shows a clear excess approximately as expected for bound binaries, with an overdense cloud following a locus $v_p \sim 1 \text{ km s}^{-1} (r_p/1 \text{ kAU})^{-0.5}$. We note that our sample starts to miss true binaries at projected separations below $r_p \lesssim 0.6 \text{ kAU}$, due to the 3 km s^{-1} velocity threshold, but this r_p is much smaller than the separations of interest below. At $r_p > 5 \text{ kAU}$ the threshold includes pairs with velocity difference far above the bound limit, which are interesting for assessing sample contamination as seen below.

It is more informative to rescale to the typical Newtonian orbit velocity, so we next estimate masses for each binary using an estimated mass/luminosity relation: here, we adopt the main-sequence $M_I(\text{mass})$ relation of *Version 2021.03.02* from Pecaut & Mamajek (2013), and the $V - I, M_I$ colour relation from the same, where M_I denotes absolute magnitude. From those we apply the colour relation given in Table C2 of Riello et al. (2021) to predict G magnitude from V and I magnitudes as

$$G \simeq V - 0.01597 + 0.02809(V - I) - 0.2483(V - I)^2 + 0.03656(V - I)^3 - 0.002939(V - I)^4 \quad (2)$$

to obtain a predicted relationship between absolute GAIA magnitude M_G vs mass; we then fit to this to obtain an approximate mass/ M_G relation

$$\frac{M}{M_\odot} = 10^{0.074(4.69 - M_G)} \quad (3)$$

Then, for each star we have M_G directly from G and parallax distance, hence an estimated mass follows. Since the luminosity(mass) relation is rather steep, small errors in G or distance have relatively little effect on mass estimates below.

For each candidate binary we then define

$$v_c(r_p) \equiv \sqrt{GM_{tot}/r_p} \quad (4)$$

as the estimated circular-orbit velocity at the current *projected* separation; for each candidate binary, we then divide the measured projected velocity difference by the above to obtain a dimensionless ratio

$$\tilde{v} \equiv v_p/v_c(r_p); \quad (5)$$

a scatter plot of this ratio is shown in Figure 3, and various histograms of this ratio are compared with models below.

2.7. Transverse velocity errors

We have estimated relative-velocity errors assuming uncorrelated errors between the two components of the binary, simply from the root-sum-square of the quoted rms errors in μ_α and μ_δ for each of the two stars in each binary, and multiplying by distance to obtain the transverse-velocity error. (This should be reasonable as long-range correlated errors should mostly cancel between the two stars).

Table 2 shows the comparison of the transverse velocity random errors between the CWB-DR2 and CWB-EDR3. We can see with the better quality of data from DR2 to EDR3, and a larger binary sample, the median has decreased to an impressively small value of $\sigma(v_p) \approx 0.06 \text{ km s}^{-1}$. We also see a decrease in values when converting to the ratio to circular-orbit velocity, $\sigma(v_p)/v_c(r_p)$, where the median for the full candidate sample has now reduced to 0.06 and the 80th percentile is 0.1; for the “wide” subsample with $5 < r_p < 20 \text{ kAU}$, the median is 0.14 and the 80th percentile is 0.26. A scatter plot of $\sigma(v_p)$ versus distance is shown in Figure 4; the trend with distance is clear, but most systems have $\sigma(v_p) \lesssim 0.15 \text{ km s}^{-1}$ even near our 300 pc limit.

The latter values are significantly smaller than 1, but not very small, so the effect of random proper motion errors will affect the detailed shape of the distributions below. However, in future GAIA data releases these values are expected to reduce by factors of at least 2–4 as proper motion precision scales as $\propto t^{-3/2}$ for fixed scan cadence, so the random errors in proper motions are likely to become relatively unimportant in the medium-term future.

We note that for a “typical” binary below at $r_p \sim 10 \text{ kAU}$ and $d \sim 180 \text{ pc}$, the angular separation is 0.27 mrad or 55 arcsec, so these are very well resolved and the uncertainty on r_p is essentially the same as the error on the mean distance, typically well below 1 percent and almost negligible. The error on v_p is dominated by random errors on the proper motions, assuming that correlated systematic errors mostly cancel between the two components of the binary. Since we are mostly interested in statistical distributions, the effect of random errors is modest as long as these are not larger than ~ 0.25 in

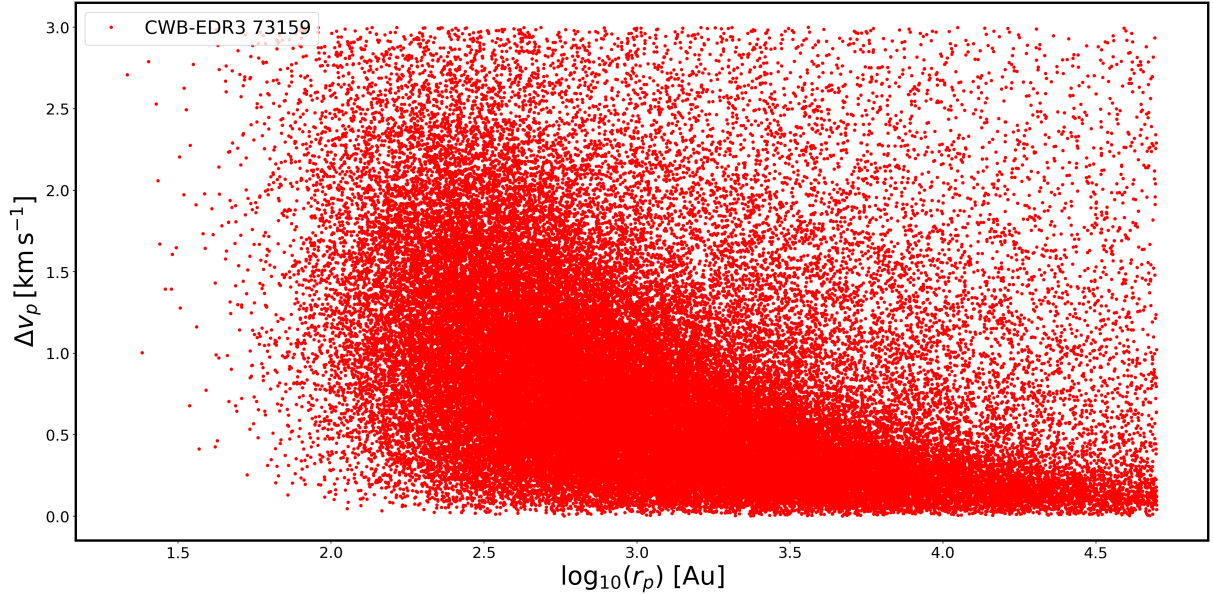


FIG. 2.— Scatter plot of projected relative velocity v_p (y-axis) vs projected separation (log scale, x-axis) for the CWB-EDR3 binary candidates. The main selection cuts are visible at top and right.

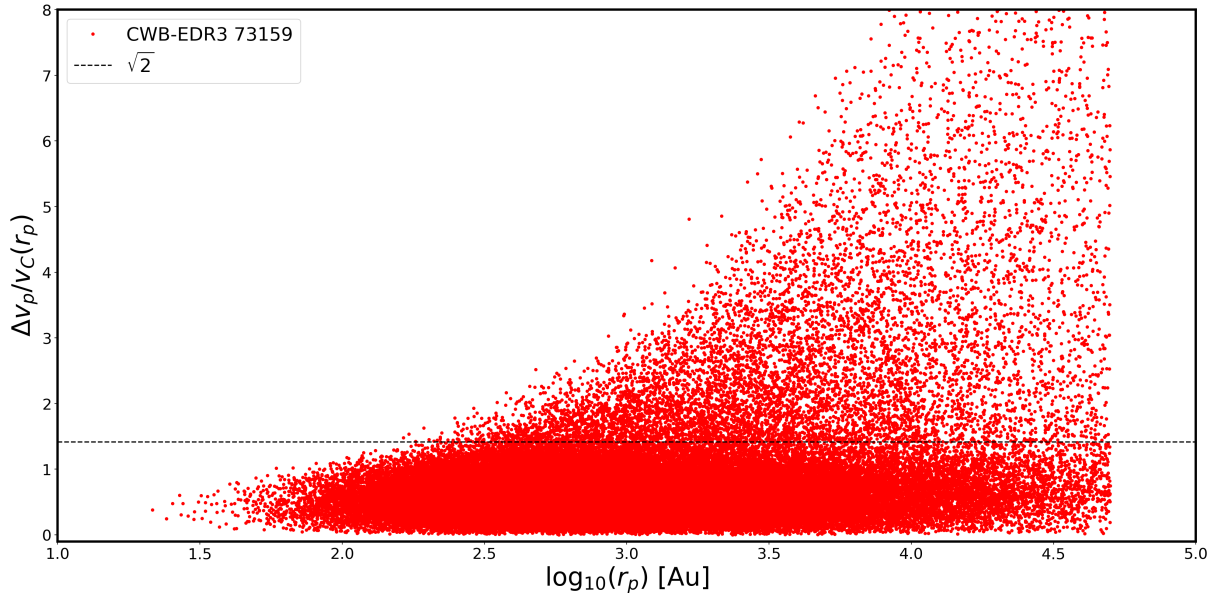


FIG. 3.— Scatter plot of projected velocity relative to Newtonian, $v_p/v_c(r_p)$, vs projected separation for CWB-EDR3 sample. The dashed line at $\sqrt{2}$ indicates the Newtonian limit. The upper cutoff is now slightly fuzzy due to the additional dependence of velocity ratio on mass. Note that in later analysis we only use the sample at $r_p > 5 \text{ kAU}$ so $\log_{10} r_p > 3.7$, so incompleteness in the upper-left region is not an issue.

$v_p/v_c(r_p)$. Note that for systems with small observed ratios $v_p/v_c(r_p) \sim 0.5$, the *fractional* uncertainty in this ratio is rather large; however such systems still have a high probability of the true ratio being $\lesssim 0.8$, so this scatter is relatively unimportant. For systems with $v_p/v_c(r_p) \gtrsim 1$, the fractional uncertainty is relatively modest; though possible non-Gaussian errors in the GAIA data remain a concern, this should improve in future GAIA releases as more observing epochs become available to reject outliers.

In summary, we note that the velocity precision for our current sample has improved over the PS19 sample, since the improved precision of GAIA EDR3 over DR2

outweighs our expanded distance and magnitude limits. The precision will continue to increase with future DR4 and beyond in the extended mission, so GAIA random errors will become negligible compared to other sources of uncertainty (especially contamination from triple systems, see below).

2.8. Comparison with El-Badry, Rix and Heintz Wide Binary EDR3 sample

Here we note that a catalogue of candidate binaries in GAIA EDR3 has been published by (El-Badry et al. 2021, hereafter ERH). Much of our sample selection was completed independently prior to the appearance of

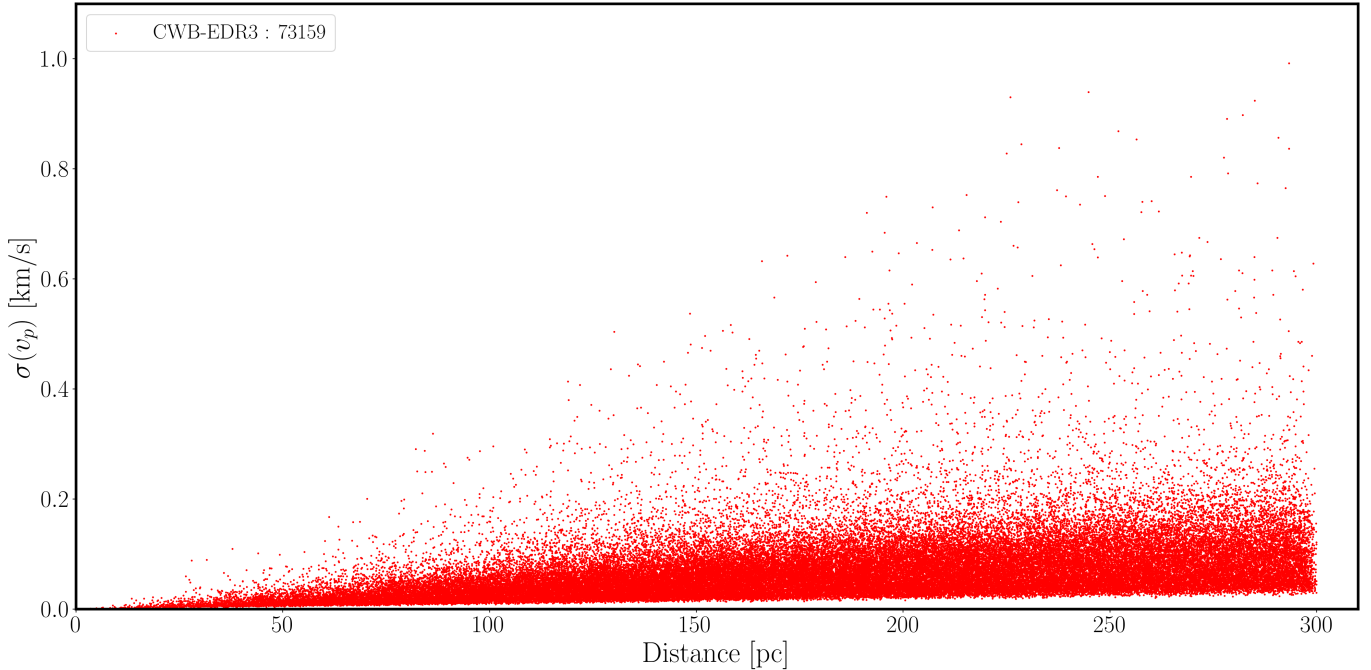


FIG. 4.— Scatter plot of rms velocity uncertainty $\sigma(v_p)$ versus mean distance for candidate binaries in CWB-EDR3.

TABLE 2

TABLE COMPARING PERCENTILES OF TRANSVERSE VELOCITY ERRORS AND RELATIVE TO CIRCULAR VELOCITY, BETWEEN CWB-DR2 (PS19) AND CWB-EDR3 DATA SETS. UPPER TABLE FOR THE FULL SETS, LOWER TABLE FOR SUBSAMPLE WITH $5 < r_p < 20$ kAU.

All r_p	CWB-DR2	CWB-EDR3
$\sigma(v_p)$ [km s ⁻¹] (50%, 80%, 90%)	≈ [0.09, 0.14, 0.2]	≈ [0.06, 0.1, 0.13]
$\sigma(v_p)/v_c(r_p)$ (50%, 80%, 90%)	≈ [0.08, 0.17, 0.26]	≈ [0.06, 0.12, 0.19]
($5 < r_p < 20$ kAU)	CWB-DR2	CWB-EDR3
$\sigma(v_p)$ [km s ⁻¹] (50%, 80%, 90%)	≈ [0.09, 0.14, 0.19]	≈ [0.05, 0.09, 0.11]
$\sigma(v_p)/v_c(r_p)$ (50%, 80%, 90%)	≈ [0.23, 0.39, 0.54]	≈ [0.14, 0.26, 0.34]

ERH, but here we give a brief comparison.

As seen in Table 3, ERH chose 1 kpc distance limit with Gaia magnitude cuts at $G \neq \text{NULL}$, while we selected our primary sample at 300 pc with $G < 17$. Note that ERH do use other cuts on relative errors, which do introduce some implicit magnitude-dependence, as fainter stars are more likely to fail those cuts. Our selection adopts a fixed projected separation of $r_p \leq 50$ kAU with parallaxes consistent within 4 times the combined uncertainty $\leq 4\sqrt{\sigma_{\bar{\omega}_1}^2 + \sigma_{\bar{\omega}_2}^2}$ and a projected velocity threshold $v_p \leq 3$ km s⁻¹ (the same as in PS19). Whereas ERH use $r_p \leq 1$ pc, with parallaxes to both members satisfying ERH

Equation 2 as follows:

$$\begin{aligned}
 |\bar{\omega}_1 - \bar{\omega}_2| &\leq b\sqrt{\sigma_{\bar{\omega}_1}^2 + \sigma_{\bar{\omega}_2}^2} \\
 b = 3, \theta_p &\geq 4'' \\
 b = 6, \theta_p &< 4''
 \end{aligned} \tag{6}$$

In addition, they apply the same separation-dependent threshold for projected velocities v_p from El-Badry & Rix (2018), which translates to $v_p \leq 2.1 \text{ km s}^{-1} (r_p/1 \text{ kAU})^{-0.5}$ (equivalent to the Newtonian bound limit $\sqrt{2} v_C$ for a $2.5 M_\odot$ system, or just above at $1.83 v_C$ for a more typical system with mass $1.5 M_\odot$). This means that our sample extends to substantially higher (unbound) velocity ratios at $r_p \gtrsim 3$ kAU, which turns out to be useful below for modelling the tail of high-velocity systems.

There are additional differences in how we cut for clusters, triples, etc, but these turn out to be relatively less important. We cut out known clusters after removing triples and hierarchical systems as described in sections 2.3, 2.2 and 2.4. In ERH, they begin cleaning by counting the number of phase-space neighbours per source from their primary selection that are brighter than $G = 18$, consistent with the size and velocity dispersion of a typical cluster. The neighbours per source are defined satisfying projected separations $r_p \leq 5$ pc and proper motions $\Delta\mu \leq 5 \text{ km s}^{-1}$, with parallaxes to both sources within $\Delta\bar{\omega} \leq 2\sqrt{\sigma_{\bar{\omega}_1}^2 + \sigma_{\bar{\omega}_2}^2}$. Any source (or either component from the binary candidate) that contains more than 30 neighbours is removed. This leads to removing all candidates where either component of the binary is a member in another binary candidate; also removing candidates that might be members of small clusters or moving groups that were not caught in the initial cleaning, performed by applying the same method in counting

TABLE 3
COMPARISON OF WIDE BINARY SELECTION BETWEEN OUR CRITERIA AND ERH21

Criteria	WB-EDR3	ERH21
Magnitude G	< 17	$\neq \text{NULL}$
Parallax $\bar{\omega}$ [mas] (d [pc])	$> \frac{10}{3} mas$ ($< 300 pc$)	$> 1 mas$ ($< 1 kpc$)
Projected Separation r_p	$\leq 50 kAU$ ($\sim 0.242 pc$)	$\leq 206.265 kAU$ ($1 pc$)
Parallax of both members $ \bar{\omega}_1 - \bar{\omega}_2 $	$\leq 4\sqrt{\sigma_{\omega_1}^2 + \sigma_{\omega_2}^2}$	$< b\sqrt{\sigma_{\omega_1}^2 + \sigma_{\omega_2}^2}$ $\begin{cases} b = 3, \theta_p \geq 4'' \\ b = 6, \theta_p < 4'' \end{cases}$
Projected velocity threshold v_p	$\leq 3 km s^{-1}$	$\leq 2.1 km s^{-1} (r_p/1 kAU)^{-0.5}$

the number of phase-space neighbours but without the magnitude cut.

We have done a cross-match of our sample to ERH as follows: we first select the subset of ERH binaries which could in principle have passed our sky, distance and magnitude criteria, i.e., where both stars have $G < 17$, galactic latitude $|b| > 15$ deg, difference in parallax distances $|d_1 - d_2| \leq 8.0 pc$, projected separation $r_p < 50 kAU$, distance to both stars $d \leq 300 pc$, parallaxes of both stars consistent with each other within $4\times$ the combined uncertainty e.g., $|d_1 - d_2| \leq 4\sigma_d$, projected velocity difference $\Delta v_p \leq 3 km s^{-1}$, and applying cuts from Arenou et al. (2018). The combination of these cuts gives a subsample of 65,234 candidate binaries from ERH which could in principle pass our other cuts, here called the ERH-cut sample. Cross-matching those against our CWB-EDR3 sample of 73,159 candidates, we find that 64,498 are in common with ERH-cut, while there are 8,661 candidates in our CWB-EDR3 but not found in ERH-cut, and 752 candidates in ERH-cut are not found in CWB-EDR3.

Figures 5 and 6 illustrate the comparisons of the 8,661 candidates in our CWB-EDR3 but not found in ERH-cut, and 752 in ERH-cut not found in CWB-EDR3. As seen in Figure 6, most of the additional binaries in our sample are either at larger velocity differences (above the ERH limit and below our $3 km s^{-1}$ limit), or at smaller separations $r_p < 0.5 kAU$ which we do not consider below.

As seen in Figure 5, the binaries in ERH-cut but not in CWB-EDR3 are largely removed due to our additional sky cuts around open clusters.

In summary we find good agreement between our sample and the ERH-cut sample, and differences in selection criteria have relatively little effect; the additional “binaries” in our sample are mostly potential triples at large velocity differences, which are useful for modelling in later sections.

3. ORBIT SIMULATIONS

In this Section we describe the simulations for predicting distributions of projected velocities in Newtonian and MOND models, for various eccentricity distributions, and for binaries, triple systems. As noted in Section 3.1 of PS19, we described how velocity ratios are handled within our orbit simulations of observables for the 2D sky-projected velocities as well as 2D projected separations; this is simply because radial velocities are not yet available for the large majority of our candidate WBs; though radial velocities may become available in future with large spectroscopic surveys such as 4MOST, PFS, WEAVE and MSE, and targeted follow-up of selected systems.

3.1. Binary orbits

Similar to Section 3 from PS19, here we simulate a large sample of $\sim 5 \times 10^6$ orbits with random values of a, e in both Newtonian gravity and one specific modified-gravity model from Banik & Zhao (2018) (hereafter BZ18).

We then study the joint distribution of observables, in particular projected separation r_p and relative velocity ratio $v_p/v_c(r_p)$, using several different eccentricity distribution functions.

In the case of modified gravity models, the orbits are generally not closed ellipses, so they are not strictly defined by the standard Keplerian parameters a, e . As in PS18 and PS19, modified-gravity orbits are parametrised using the “effective” orbit size \hat{a} and quasi-eccentricity \hat{e} as follows: we define \hat{a} to be the separation at which the simulated relative velocity is equal to the circular-orbit velocity (in the current modified-gravity model), then we define θ_{circ} to be the angle between the relative velocity vector and the tangential direction when the orbital separation crosses \hat{a} , and then $\hat{e} \equiv \sin \theta_{\text{circ}}$; these definitions coincide with the usual Keplerian a, e in the case of standard gravity.

For the eccentricity distributions, we choose 3 example cases: first a flat distribution $f(\hat{e}) = 1$; second the distribution fitted by Tokovinin & Kiyaveva (2016), $f(\hat{e}) = 0.4 + 1.2\hat{e}$; and thirdly the thermal distribution $f(\hat{e}) = 2\hat{e}$. We note here some other recent studies: Tokovinin (2020) and Hwang et al. (2022) have studied the eccentricity distribution of wide binaries by fitting the observed distribution of angles between the sky-projected separation and sky-projected relative velocity; the inferred distributions are clearly rising with e . At large separations, both studies favour a somewhat super-thermal distribution, $f(e) \propto e^{1.35}$; however the difference in predictions between this and the thermal distribution is relatively modest, with median e values 0.7071 for the thermal distribution versus 0.745 for $f(e) \propto e^{1.35}$. (We do not use relative angles in the fitting below, though in principle this contains additional information).

After integrating these orbits using either of the above gravity laws (Newton/GR, Realistic MoND Model with ExFE as described in BZ18) and a chosen value for external field $g_e \sim 1.2a_0$, we “observe” the resulting binaries at many random times and random inclinations to the line-of-sight.

For each simulated orbit/epoch snapshot, we produce simulated observables including the projected separation r_p , projected relative velocity v_p , and also $v_p/v_c(r_p)$ corresponding to our observables from Gaia.

The radial acceleration law is chosen according to the selected gravity theory under consideration with the External Field Effect (ExFE) on (see below). For the New-

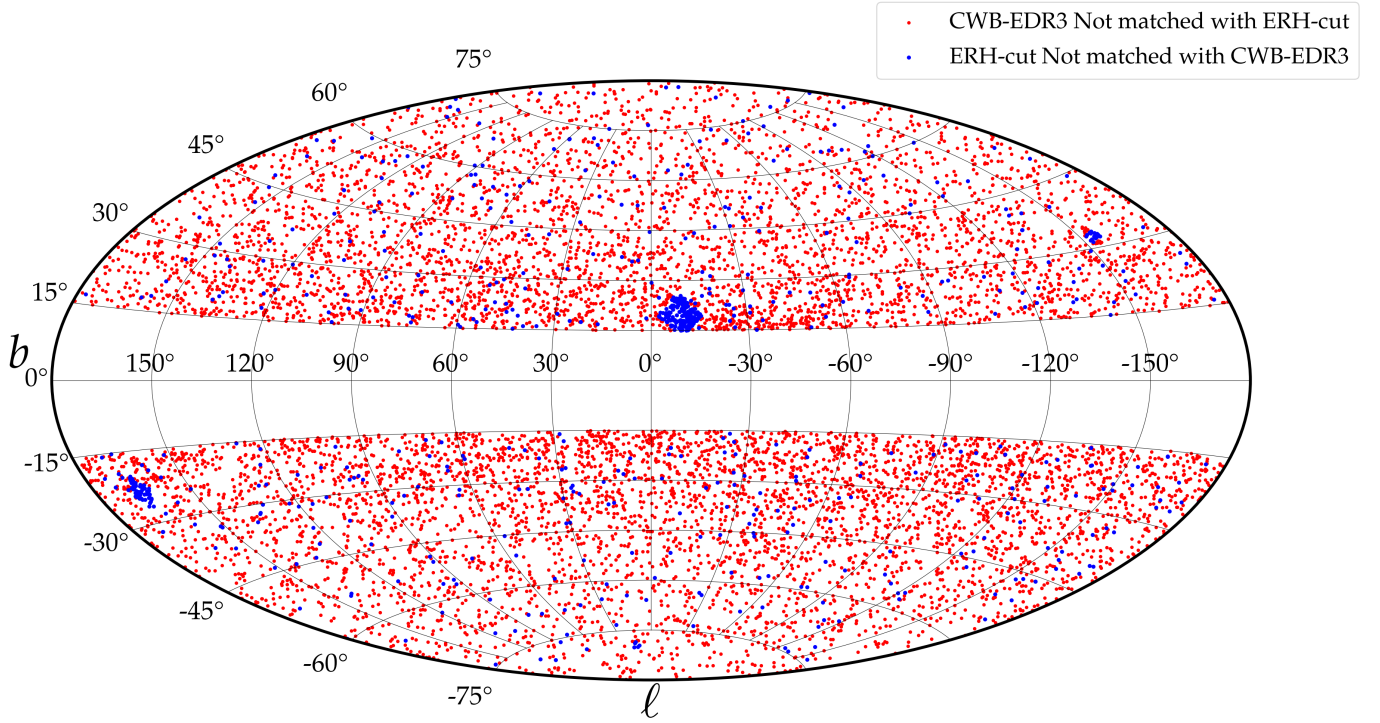


FIG. 5.— Aitoff projection of CWB-EDR3 binaries not found in ERH-cut sample (red points), and binaries from ERH-cut not found in CWB-EDR3 (blue points).

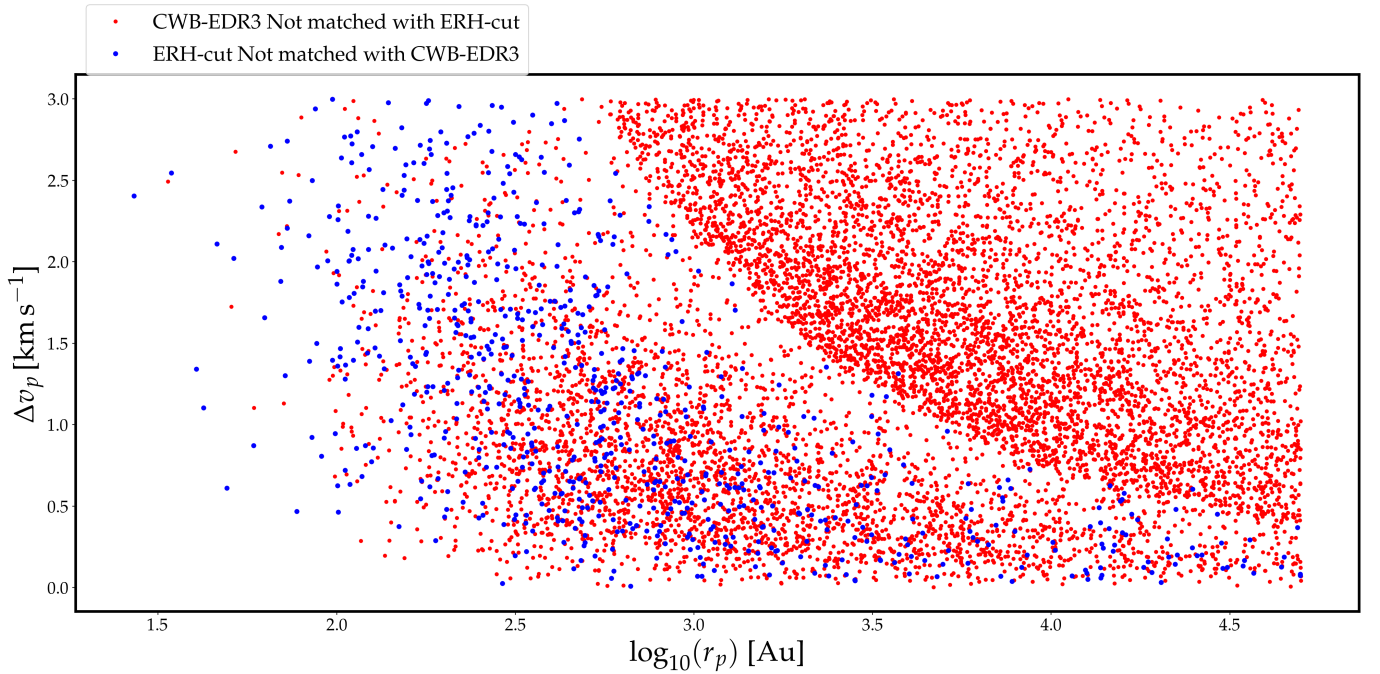


FIG. 6.— Scatter plot of projected velocity difference Δv_p vs projected separation for CWB-EDR3 binaries not found in ERH-cut sample (red points), and binaries from ERH-cut not found in CWB-EDR3 (blue points).

tonian/GR case, we have the standard

$$g_N = \frac{G(M_1 + M_2)}{r^2} \quad (7)$$

For the MOND-like case with ExFE, we use the fitting function of [McGaugh \(2016\)](#) (hereafter MLS), sometimes known as the “radial acceleration relation”, given by

$$g_{MLS} = g_N \nu(g_N/a_0); \quad (8)$$

$$\nu(y) = \frac{1}{1 - \exp(-\sqrt{y})};$$

we refer to this ν function as the MLS interpolating function below. This function is shown by MLS to produce a good fit to rotation curves for a large sample of disc galaxies spanning a range of masses; it also has the desirable feature that the function $\nu(y)$ converges very rapidly to 1 when $y \gtrsim 20$, so deviations on Solar System scales are predicted to be vanishingly small, consistent with observational limits.

The only modified-gravity model we consider to compare against our CWB-EDR3 sample is the MOND model with ExFE, using the approximation of [BZ18](#); this is given by

$$g_{N,int} = G(M_1 + M_2)/r^2 \quad (9)$$

$$g_{N,gal} = 1.2 a_0 \quad (10)$$

$$g_{N,tot} = (g_{N,int}^2 + g_{N,gal}^2)^{1/2} \quad (11)$$

$$g_{i,EFE} = g_{N,int} \nu(g_{N,tot}/a_0) \left(1 + \frac{\kappa(g_{N,tot})}{3} \right) \quad (12)$$

$$\kappa \equiv \frac{\partial \ln \nu}{\partial \ln g_N} \quad (13)$$

where $g_{N,int}$ is the internal Newtonian acceleration of the binary; $g_{N,gal}$ is the external (Galactic) Newtonian acceleration, $g_{N,tot}$ is the quadrature sum of these, ν is the MLS function from Equation (8) and $g_{i,EFE}$ is our model MOND-ian internal acceleration, approximating the application of the external field effect. (This is not quite an exact solution of the MOND-like equations, but is shown by [BZ18](#) to be a good approximation to the full numerical solution).

Above, the observed Galactic rotation values $v_{LSR} \simeq 232 \text{ km s}^{-1}$ and $R_0 \simeq 8.1 \text{ kpc}$ imply a total Galactic acceleration close to $1.75 a_0$, hence we require $g_{N,gal} \nu(g_{N,gal}/a_0) \approx 1.75 a_0$. Solving this leads to $g_{N,gal} \approx 1.16 a_0$ as above and $\nu \approx 1.51$, in reasonably good agreement with the estimated baryonic contribution to the Galactic rotation (as expected, since the MLS fitting function was derived by fitting to a sample of external spiral galaxies with well-observed rotation curves, so this is consistent with our Galaxy being typical).

As in [PS19](#), at wide separations beyond 7kAU, this specific modified gravity model produces typical accelerations which saturate at $\approx 1.35 \times$ larger than Newtonian, and thus binary orbital velocities boosted by $\sim 16\%$.

In Figure 8, we show histograms of the ratio $v_p/v_C(r_p)$ for four bins of projected separation, and two gravity acceleration models: standard Newtonian, and the Banik $\sim 1.2 a_0$ Realistic ExFE from [BZ18](#); and a 3-Body Newtonian model compared with the GAIA CWB-EDR3 and CWB-DR2 samples. Model histograms are scaled to

match the total of the data at velocity ratio $\leq \sqrt{2}$.

On inspection of Figure 8, several features are notable:

1. The observed histograms all show a clear peak at a ratio ~ 0.6 , in rough agreement with either Newtonian gravity or our MOND model. The shape of the peak is sensitive to both the eccentricity distribution than the gravity model, with flat $f(e)$ giving a slightly pointed peak, while $f(e) = 2e$ makes the peak more rounded and shifted to a slightly lower value.
2. Comparing to results from PS19 (not reproduced here), we found that simulated histograms for MOND *without* ExFE showed a large and obvious shift of the peak to larger velocity ratios $\gtrsim 1$, especially in the wider separation bins where the Newtonian acceleration is well below a_0 ; such a large shift in the peak appears clearly inconsistent with the data, so we confirm the conclusion of PS19 that MOND *without* ExFE is firmly excluded (though this was already disfavoured on theoretical grounds).
3. The simulated histograms for MOND *with* ExFE show a distinctly larger fraction of binaries at velocity ratio 1.1 – 1.5, compared to the Newtonian cases; that excess is rather insensitive to the $f(e)$ distribution, increasing only moderately with projected separation. So as in PS18, this region is the key discriminant between Newtonian vs MOND models.
4. The actual data show a clear peak at ~ 0.6 as above, then a fall towards $\sqrt{2}$; however this is followed by a prominent tail which slowly declines to much larger ratios $\gtrsim 5$. Clearly, the presence of this tail makes it hard to decide a preference between Newtonian or MOND-with-ExFE: a smooth downward extrapolation of the tail below $\sqrt{2}$ can account for a significant fraction of observed systems at velocity ratio $1.1 < v_p/v_C(r_p) < 1.4$, so the tail is not well understood but has a major impact on the statistics. This tail is discussed and modelled in the next Section.

3.2. Triple system simulations

As we can see from the histograms in Figures 7 and 8, the observed CWB-EDR3 sample has a velocity distribution described qualitatively by a “hump+tail” shape very similar to [PS19](#). In [PS19](#), we selected random “binaries” from copies of the DR2 catalogue with sky positions randomised by a few degrees; this showed that the “tail” is much too populous to explain as random chance projections of unassociated stars; we verify this for our new sample in 3.3 below. The next alternative was the possibility of co-natal stars born in the same open cluster, which is currently dissolving therefore, having similar velocities and undergoing chance flybys. Although this provided acceptable χ^2 values, there was a potential inconsistency in that the fitted number of flyby events was decreasing with r_p , while simulations predict a rising distribution, due to the increasing phase-space volume at larger projected separation. It was then suggested by

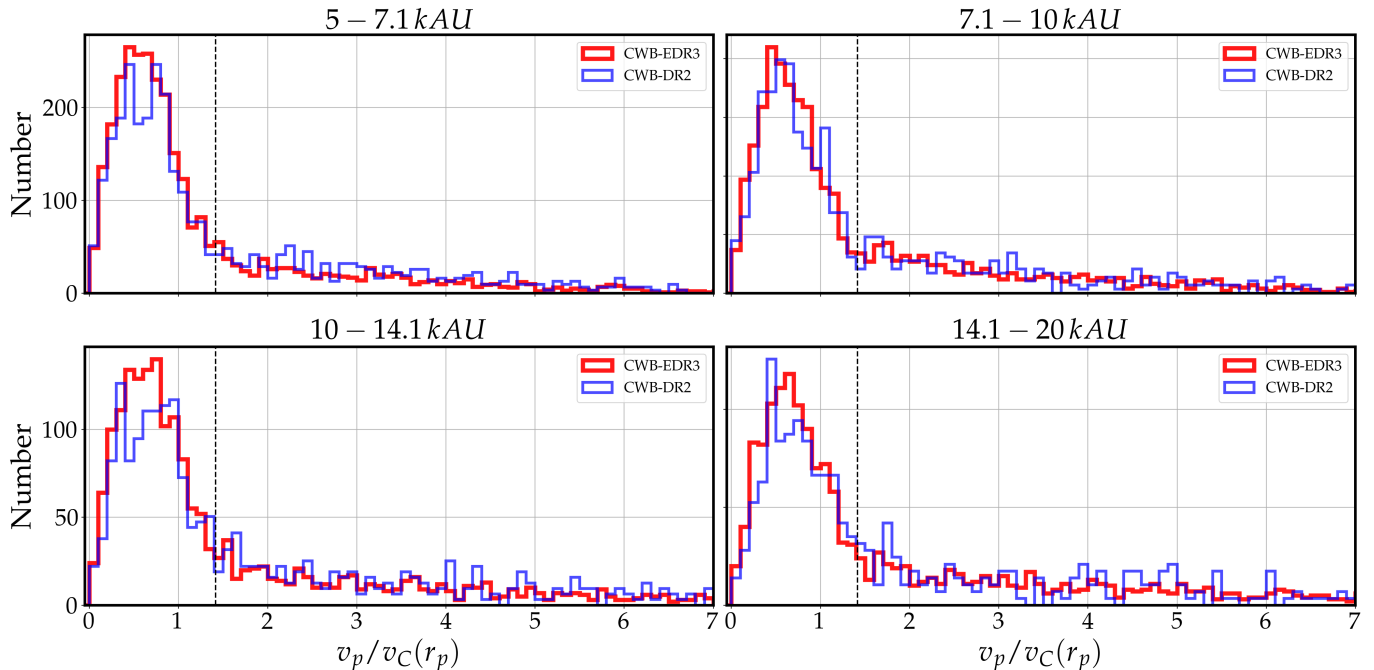


FIG. 7.— Histograms of velocity ratio, $v_p/v_C(r_p)$, for observed binaries: the four panels show four bins of projected separation as labelled above each panel. The histograms shows our observed CWB-EDR3 (red) and the CWB-DR2 (blue) sample; numbers in the latter are renormalised to match the total number in the CWB-EDR3 sample.

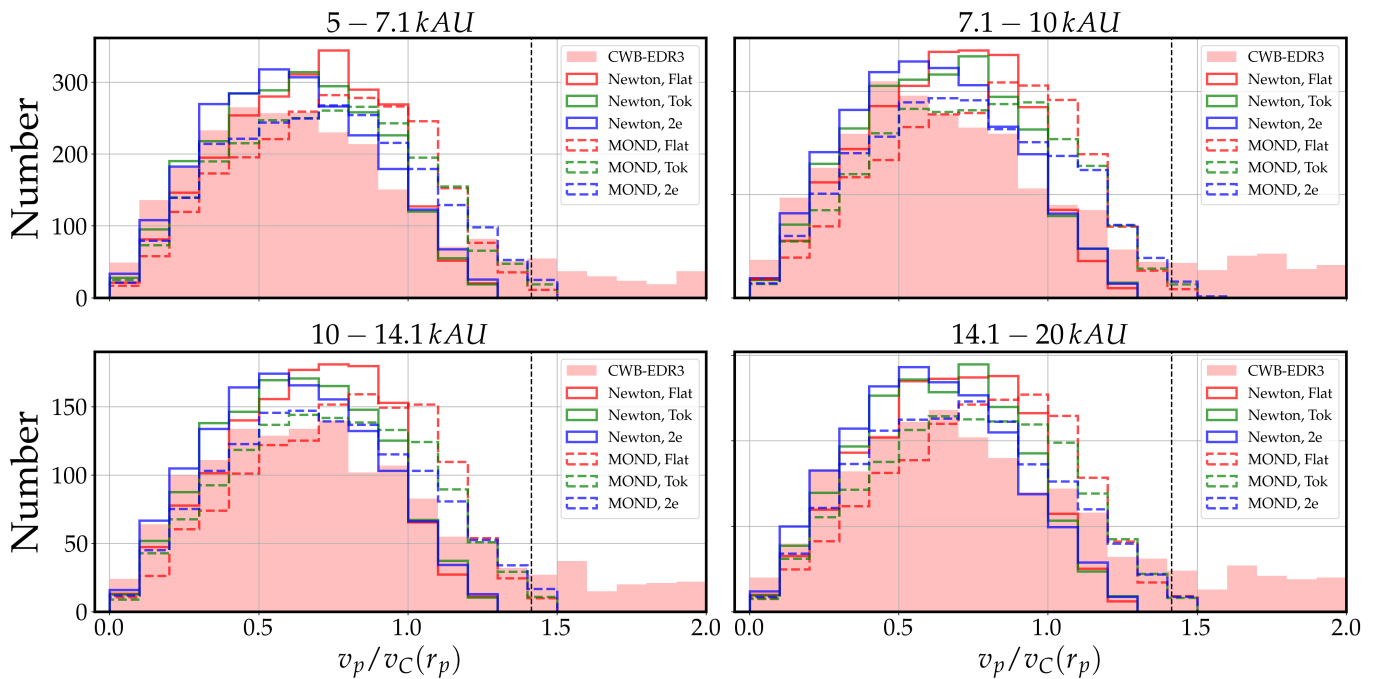


FIG. 8.— Histograms of velocity ratio, $v_p/v_C(r_p)$, for observed and simulated binaries (simulated binaries are pure 2-star systems excluding triples and flybys): the four panels show four bins of projected separation as labelled in the legend. The shaded pink histogram shows our observed CWB-EDR3 (red); solid lines show Newtonian orbits, and dashed lines for the MOND model. Line colours show eccentricity distribution: flat $f(e) = 1$ (red), Tokovinin (green) and $f(e) = 2e$ (blue). Simulated histograms are normalised to the number of observed systems at ratio ≤ 1.6 .

Clarke (2020) that triple systems with an unseen or unresolved third star could account for the tail, and the simulated distribution was found to produce a good fit to the tail, though the fraction of triples required is quite large (fixed at 50 percent in Clarke (2020)). Below, we will model the observed distribution with a mixture of binary, triple and flyby systems.

To simulate the triple systems, we generate two binary orbits made up of three stars. We label star 1 as the single star, and stars 2 & 3 as the inner binary, so the outer orbit is star 1 orbiting the barycentre of stars 2 and 3. We choose random masses for the three stars with a flat distribution up to $0.7 M_{\odot}$, then declining as $m^{-2.35}$; we pick three random masses, relabel so that $M_2 > M_3$, and apply the constraint that stars 1 and 2 are $\geq 0.5 M_{\odot}$, while star 3 is $\geq 0.01 M_{\odot}$ and may be unobservable.

For orbit sizes, we choose the outer orbit size \hat{a}_{out} from a flat distribution in $\log_{10}(\hat{a}_{out}/1 \text{ kAU}) \in (0, 2)$, and the inner orbit size \hat{a}_{inn} is chosen from a flat distribution in $\log_{10} \hat{a}_{inn}$, with a minimum at 0.1 AU and a maximum at $0.3 \times$ the outer orbit; this is an approximate criterion for long-term stability.

We generate eccentricities from one of three distributions: either flat $f(e) = 1$, an intermediate case from Tokovinin & Kiyaveva (2016) (hereafter Tokovinin), and $f(e) = 2e$. Both inner and outer eccentricities use the same distribution function, but drawn independently of each other.

For simplicity, we treat the inner and outer orbits as independent. We solve for the two orbits independently in their own planes, and then apply a random 3D rotation matrix, \mathbf{R} , to the inner orbit relative velocity to generate a random relative alignment between the two orbits. Next the system is “observed” at 10 random phases and 10 random viewing directions for each phase. At each simulated “observation” we evaluate the projected separation, and the 3D velocity difference between star 1 and the “observable center” of stars 2+3, as follows.

$$\mathbf{v}_{3D,obs} = \mathbf{v}_{out} - f_{pb} \mathbf{R} \mathbf{v}_{inn} \quad (14)$$

where \mathbf{v}_{out} is the outer orbit velocity (star 1 relative to the barycentre of 2+3), and \mathbf{v}_{inn} is the relative velocity between stars 2+3. The latter velocity is rotated and scaled down by a dimensionless factor $f_{pb} \leq 0.5$, defined as the fractional offset between the “observable centre” and the barycentre of stars 2+3, relative to their actual separation. The “observable centre” is defined according to the angular separation: if less than 1 arcsec, we assume stars 2+3 are detected by GAIA as a single unresolved object, and use the luminosity-weighted centroid (photo-centre) of the two. Otherwise for separation > 1 arcsec, we assume stars 2 and 3 are detected as separate objects, or star 3 is unobservably faint, and we take the position of star 2 alone as the observable centre. Therefore, this results in a fractional offset

$$f_{pb} = \begin{cases} \frac{M_3}{M_2+M_3} - \frac{L_3}{L_2+L_3} & (\theta < 1 \text{ arcsec}) \\ \frac{M_3}{M_2+M_3} & (\theta \geq 1 \text{ arcsec}) \end{cases} \quad (15)$$

where the $L_{2,3}$ are the model luminosities.

The 3D velocity above is then converted to 2D projected velocity according to the random viewing direction, and observables are saved to create simulated histograms for triple systems; this procedure is repeated for

both of the gravity models (Newtonian / MOND) and each of the three eccentricity distributions. These simulated triple results are then used in the fitting procedure below.

3.3. Random Samples

Using the same method as described in Section 3 of PS19, we estimated the level of contamination of our CWB-EDR3 sample by random chance projections of unrelated stars which just happen to contain small velocity differences. We constructed several randomised samples by starting with our single-star PEDR3 sample, removing one star from each binary, then randomising the RA/Dec values individually by a few degrees (e.g., randomising within $\in \pm 3$ deg); these position shifts preserve global distributions with respect to galactic coordinates, but large enough to eliminate most truly associated stars; we then re-ran the binary search on the position-randomised samples. The number of random “binaries” was small in each single run, so we repeated 9 times with different random seeds and averaged.

We show an example histogram for a set of randomised samples compared to our observed CWB-EDR3 data in Figure 9; here the mean of random samples is multiplied by $10 \times$ for visibility, since the number of randoms is much smaller than the observed data and difficult to see in the histogram.

The main result from our randomised samples is that they contain far fewer candidate “binaries” than the observed CWB-EDR3, hence observed data greatly outnumber the randoms. As we can see, the randomised sample show no peak at small velocity ratios, but a fairly smooth distribution with a gradual rise towards larger velocity ratios. We get the same result as PS19 that the “tail” distribution of the observed data is much more populous than our randomised samples, hence the “tail” cannot be due to chance projections of unrelated stars.

3.4. Flyby simulations

We find below that fitting purely with binary+triple systems gives reasonable fits, but requires a somewhat improbable result that the ratio of triples to binaries is steeply increasing towards larger projected separations. As in PS19, we therefore model an additional population of “flyby” systems which have small velocity differences (e.g. co-natal stars born in the same birth cluster) on unbound hyperbolic flyby trajectories.

Similar to PS19, our randomised-position samples show that the tail is much too populous to be explained by random chance projections of unrelated stars; one plausible explanation appears to be pairs of co-natal stars born in the same open cluster, which therefore have similar velocities and are currently undergoing a chance close flyby. Evidence for a population of such “cold streams” has been given by Oh et al. (2017).

In this case, we would expect two of the three velocity components (perpendicular to the escape direction) must be similar in order to get a close flyby, while the velocity difference in the escape direction should approximately reflect the distribution in ejection velocities from the cluster and the time difference between the two ejections.

During a flyby, the relative velocity will speed up according to a hyperbolic flyby orbit. To simulate this, we

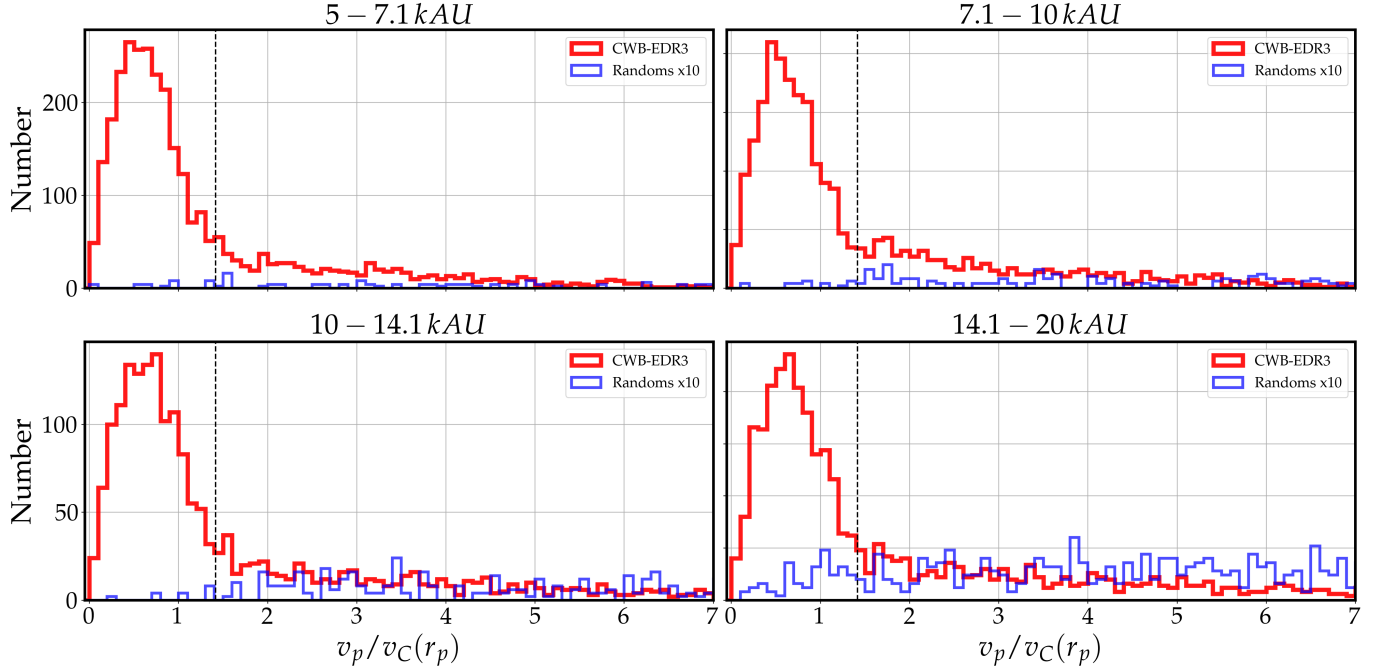


FIG. 9.— Histograms of velocity ratio $v_p/v_C(r_p)$ for observed and randomised sample. The four panels show four bins of projected separation as titled. The histograms show our observed CWB-EDR3 (red), and the mean of 9 randomised samples (blue), with the mean random sample artificially scaled-up by $10\times$ to enhance visibility.

generated random flyby encounters as follows:

1. We chose a distribution of impact parameter b with $dn/db \propto b$ up to a maximum value of 300 kAU or 1.45 pc.
2. We chose a distribution of asymptotic velocity difference v_∞ uniform up to 2 km s^{-1} .
3. Given random values of b, v_∞ generated as above, each such pair produces one flyby encounter. We sampled each hyperbolic flyby at random times while the 3D separation was $\leq 300 \text{ kAU}$, and computed the 3D relative separation and relative velocity vectors. We “observed” these from random viewing angles to produce v_p, r_p .
4. We truncated the sample as for the DR2 data, at $r_p < 40 \text{ kAU}$ and $v_p \leq 3 \text{ km s}^{-1}$, and computed the resulting velocity ratio $v_p/v_c(r_p)$.

For hyperbolic flyby encounters the 3D velocity ratio $v_{3D}/v_c(r)$ is always $\geq \sqrt{2}$, with the simulations showing a modest pile-up in the distribution just above this value; this pile-up arises from flybys with eccentricity not much larger than 1, which speed-up substantially but have velocity ratios decreasing towards $\sqrt{2}$ as they approach pericenter. The projection to 2D separation and velocity smears this distribution towards lower ratios, and therefore fills-in the gap below $\sqrt{2}$; the result is that simulated fly-bys with a flat distribution of v_∞ produce a smooth maximum in the distribution at a ratio below 1.0, with a gently declining tail at larger ratios, as shown in the next section.

4. DATA VS MODEL COMPARISONS

In this section we fit the observed distributions of $v_p/v_C(r_p)$ in our EDR3 wide-binary sample as a mixture of binary, triple and flyby systems, where the velocity distribution for each is given by the results of the simulations in Section 3. (Thus, this is a generalised case between Clarke (2020) who fitted binaries+triples, and PS19 which fitted binaries + flybys.)

Here, we have applied an additional cut to the sample based on the “Renormalised Unit Weight Error” or **ruwe** parameter defined in GAIA EDR3; this is a measure of scatter of individual GAIA observations around the basic 5-parameter fit parallax + uniform proper motion, scaled so the median **ruwe** is close to 1. Objects with a **ruwe** value significantly larger than 1.4 are indicative of excess scatter which may indicate a poor fit or a marginally-resolved close pair. Therefore, we apply an additional cut that both stars in a candidate binary are required to have **ruwe** < 1.4 . This reduces the wide-binary sample ($5 \text{ kAU} \leq r_p \leq 20 \text{ kAU}$) from 9063 systems to 7276 systems, but significantly reduces the fraction in the high-velocity tail at $\tilde{v} > 1.4$; of the 1787 pairs rejected by the **ruwe** cut, 68% had $\tilde{v} > 1.4$; while of the 7276 surviving systems, only 24% have $\tilde{v} > 1.4$.

We take the four bins as above in projected separation, and fit independently to the observed \tilde{v} distribution in each separation bin.

As noted earlier, we found that fitting with only binary+triple systems can produce reasonable fits to the data (in agreement with Clarke (2020)), but has a problem in that the fitted ratio of triple to binary systems is steeply increasing with r_p ; the fitted population ratio (number of triples)/(number of pure 2-star binaries) is 1.25 in the smallest r_p bin, but increases to around 2.75 in the widest r_p bin; this is because the “tail” becomes

relatively more populous relative to the “hump” with increasing r_p , and the tail is completely fitted by triples since there are no binaries above ratio 1.41 in Newtonian gravity, or 1.6 in MOND. We therefore modified the fitting to include an additional population of “flyby” systems as in Section 3.4, which naturally tends to increase with r_p .

This leads to an issue in that the triple and flyby populations are somewhat degenerate with each other since they both produce similar shapes in the “tail”, so we then fixed the triple/binary population ratio at a constant value; we explored fits with ratio of (triple systems)/pure 2-star binaries) set to 0.5, 0.8 or 1.0, and found that 1.0 is marginally preferred, so results below are for this value. We then repeat the fitting for each separation bin with two gravity models and three eccentricity distributions, for a total of $2 \times 3 \times 4$ independent fits. Each fit has only two adjustable parameters, the total number of pure-binary systems and the total number of flyby systems; we hold the ratio of triple to pure-binary systems fixed at a selected constant value, here 1.0. The shape of each of those is constrained at the output of the simulated orbits, for the corresponding gravity model and eccentricity distribution. We then simply fit the number in each population to minimise the χ^2 residuals between binary+triple+flyby model and the data.

The fitting range is $0 \leq \tilde{v} \leq (5, 6, 7, 7)$ respectively in the four r_p bins; these upper limits are chosen because our 3 km s^{-1} velocity cutoff leads to some incompleteness for higher-mass binaries at smaller $r_p \sim 5 \text{ kAU}$ and high $\tilde{v} \geq 5$. At our 90th percentile system mass of $2.02 M_\odot$, 3 km s^{-1} maps to velocity ratio $\tilde{v} = 5.0\sqrt{(r_p/5 \text{ kAU})}$ so our 3 km s^{-1} threshold includes nearly all systems up to the above \tilde{v} limits.

The results of the fitting procedure are shown in Figures 10 - 15 below. Here Figures 10 - 12 show the fits with Newtonian gravity and the three simulated eccentricity distributions (flat, Tokovinin, $2e$) respectively, and Figures 13 - 15 show the corresponding results for the specific modified-gravity model described in Sec. 3.1, and the same three eccentricity distributions.

Some selected values from the fitting results are listed in Tables 4 - 9; for each separation bin and model, this lists the observed numbers of EDR3 systems and fitted number of binary, triple and flyby systems, in three selected ranges of \tilde{v} : firstly $0 \leq \tilde{v} < 7$, secondly $0 \leq \tilde{v} \leq 1.4$, and also $1.1 \leq \tilde{v} \leq 1.4$, with the latter range being particularly sensitive to modified-gravity effects.

The overall goodness of fit χ^2 values are listed in the Tables and plotted versus projected separation bin in Figure 16; since the bins are width 0.1 and \tilde{v} upper limits are respectively 5,6,7,7, there are respectively 50, 60, 70, 70 datapoints in the four separation bins. The result seen in Figure 16 is that all four separation bins show a common ordering, with Newtonian gravity and $2e$ eccentricity distribution giving the best fit, and MOND with flat $f(e)$ giving the worst. Interestingly, all three Newtonian fits give a lower χ^2 value than the best of the MOND models (also $f(e) = 2e$). Therefore, since our three eccentricity models span the range expected for any reasonably smooth distribution, the fact that we do not know the true eccentricity distribution seems not to be a serious problem for the future development of

this test.

On inspection of the data and model histograms in Figs 10 - 15, it is clear that a substantial part of the difference is due to the region around velocity ratios $1.0 \leq \tilde{v} \leq 1.5$, where all of the MOND fits overshoot the observed data values by a significant margin. This region was already highlighted as a key discriminant in PS18, since MOND predicts a substantially higher fraction of true binaries in this range compared to Newtonian gravity. Therefore, the predicted “MOND excess” in this range appears **not to be present in the data**, which will become a serious problem for MOND if our modelling of the triple + flyby populations proves realistic. We are not yet confident in our modelling of the triple + flyby or other populations, but hope to improve this in future work.

The formal significance of the preference for Newtonian gravity over MOND is very high, with the best Newtonian model ($2e$) having $\Delta\chi^2 \simeq -246, -164, -56, -60$ respectively in the four bins compared to the best MOND model (also $2e$); the absolute χ^2 values are acceptable for our best Newtonian model in the two wider bins, but not in the two narrower bins, so the formal significance should not be overstated.

4.1. Caveats and Limitations

Within the limited scope of the modelling above, the data shows a fairly strong preference for Newtonian gravity over our one MOND version. However, there are several caveats and limitations which we discuss below.

1. Perhaps the major caveat here is that our triple model is only a single realisation for each eccentricity distribution: for all other parameters we have taken a principle of “maximum randomness” with uncorrelated masses, e values, inclinations and orbit ratios between inner and outer orbits. If the real triple population deviates from this simple assumption, then the predictions for the velocity distribution in triples will vary accordingly, and this will change the fit results. However, we note that in order to improve the MOND fits, it is hard to change the shape of the model distribution for the pure binaries; for pure binaries, assuming random phases and inclinations the model distribution is entirely determined given the $f(e)$ distribution function, and we have already explored reasonable limiting cases for this. Therefore, to improve the MOND fits we would need the triple+flyby models to produce fewer systems than our model in the range $1.0 \leq \tilde{v} \leq 1.5$, while maintaining the shape in the tail at $\tilde{v} > 1.5$; this may be challenging, but remains to be explored.
2. Another limitation is that we have only explored a single realisation of MOND and a simplified treatment of the external field effect; there are many variants of MOND-like models in the literature (see e.g. Barrientos et al. (2018) for examples). While the total acceleration law for a viable MOND is reasonably well constrained by the requirement to match observed disk galaxy rotation curves, the external field effect may vary between models; if the actual external field effect produces stronger con-

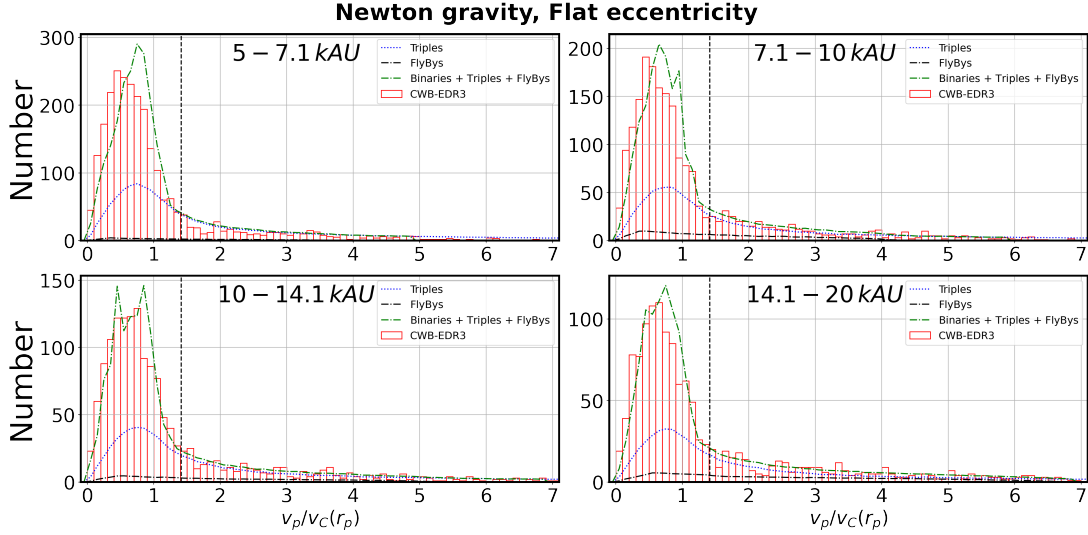


FIG. 10.— Fits of velocity ratios using the Binaries+Triples+FlyBys model for Newtonian gravity and all orbits drawn from a flat eccentricity distribution. The four panels show four bins of projected separation as labelled. The red histogram shows the CWB-EDR3 data. The blue-dotted line is the fitted triple population; black half-dashed line are the FlyBys; green dashed line is the total, so the difference is fitted true binaries.

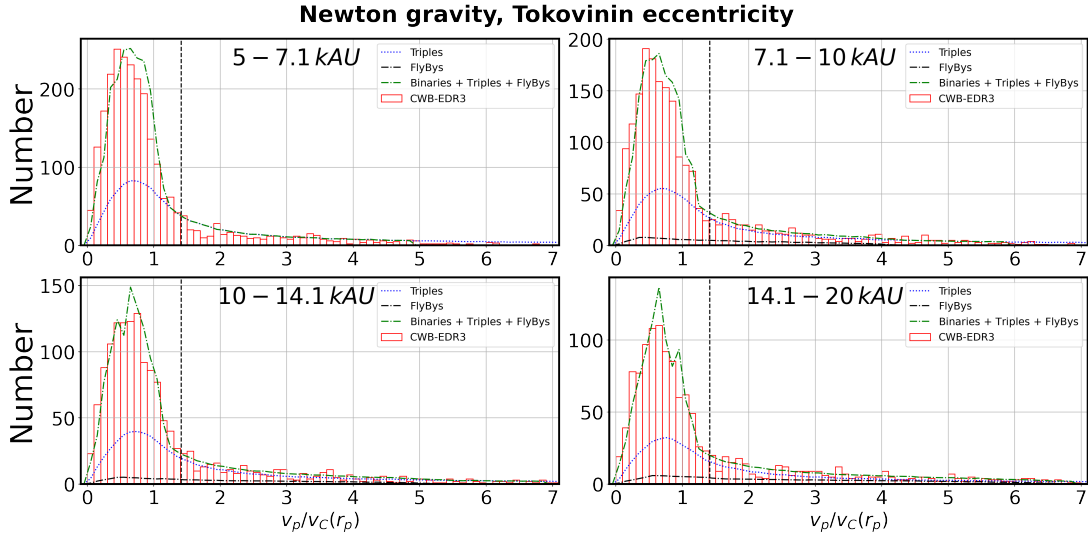


FIG. 11.— Same as Figure 10, except that model orbits are drawn from a Tokovinin eccentricity distribution.

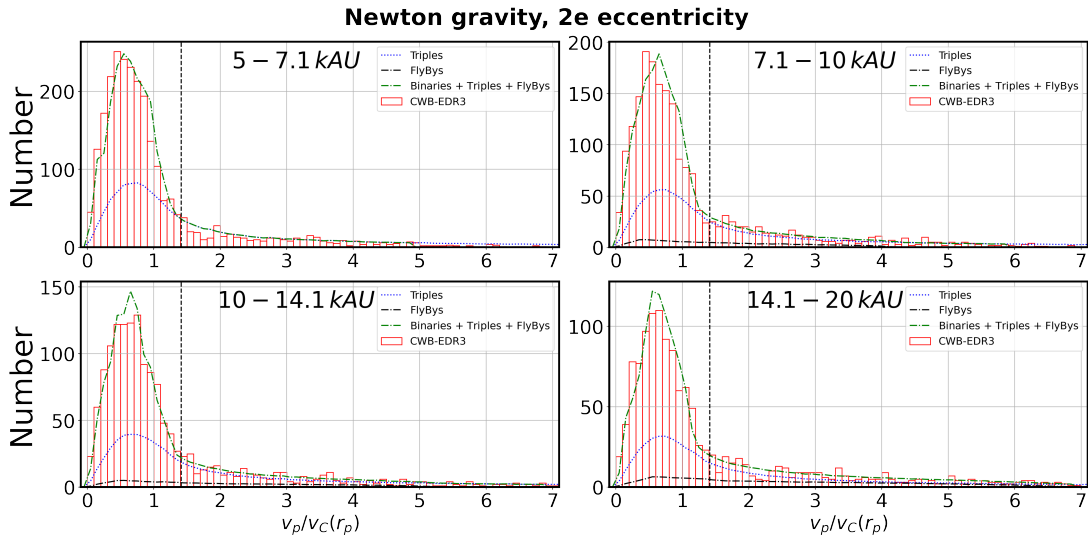


FIG. 12.— Same as Figure 10 with Newtonian gravity, but model orbits are drawn from a $f(e) = 2e$ eccentricity distribution.

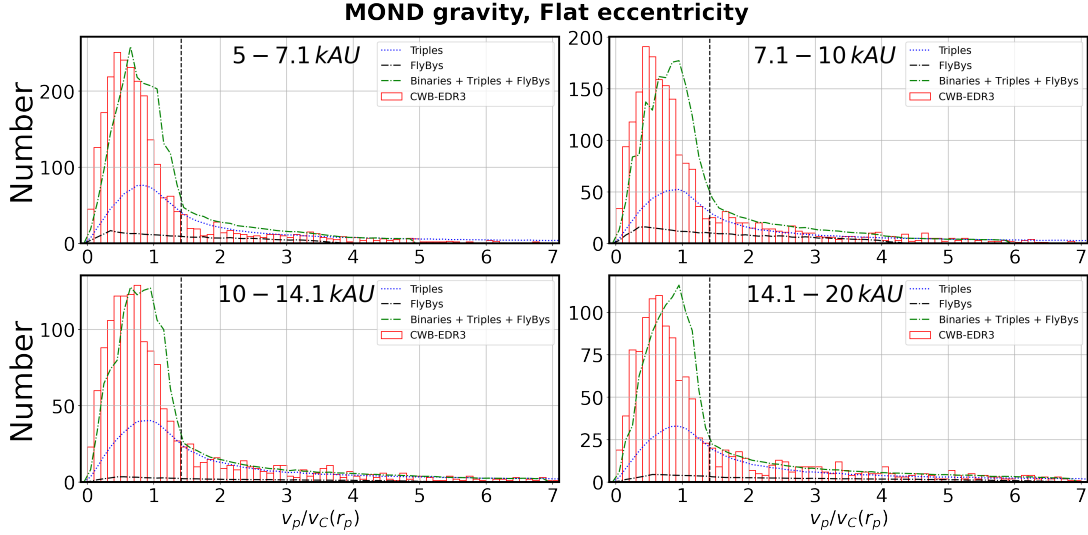


FIG. 13.— Same as Figure 10, but using the realistic MOND gravity model of Sec. 3.1 and all orbits drawn from a flat eccentricity distribution.

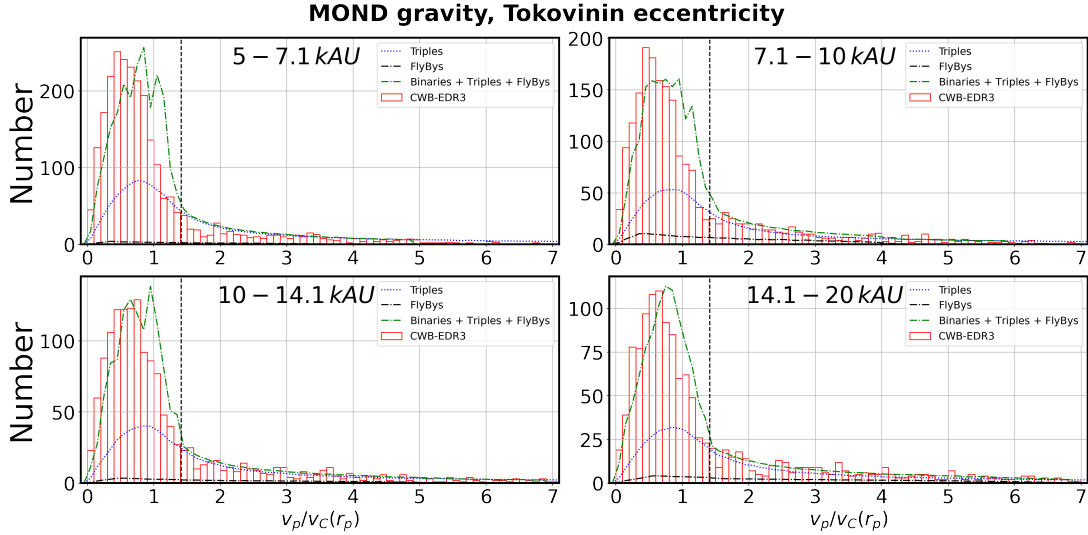


FIG. 14.— Same as Figure 13, with realistic MOND gravity model and model orbits drawn from a Tokovinin eccentricity distribution.

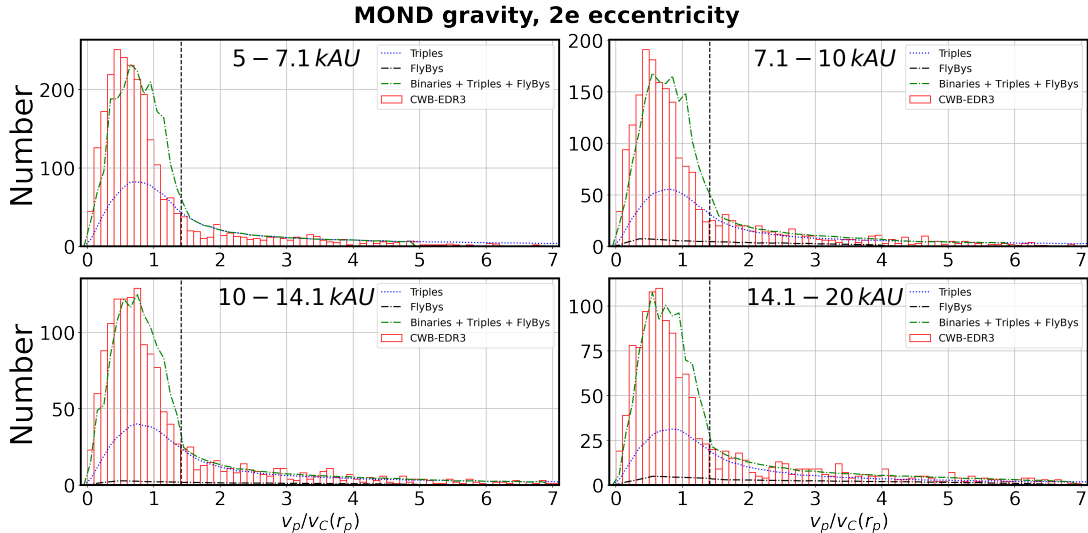


FIG. 15.— Same as Figure 13, with realistic MOND gravity model and model orbits drawn from an $f(e) = 2e$ distribution.

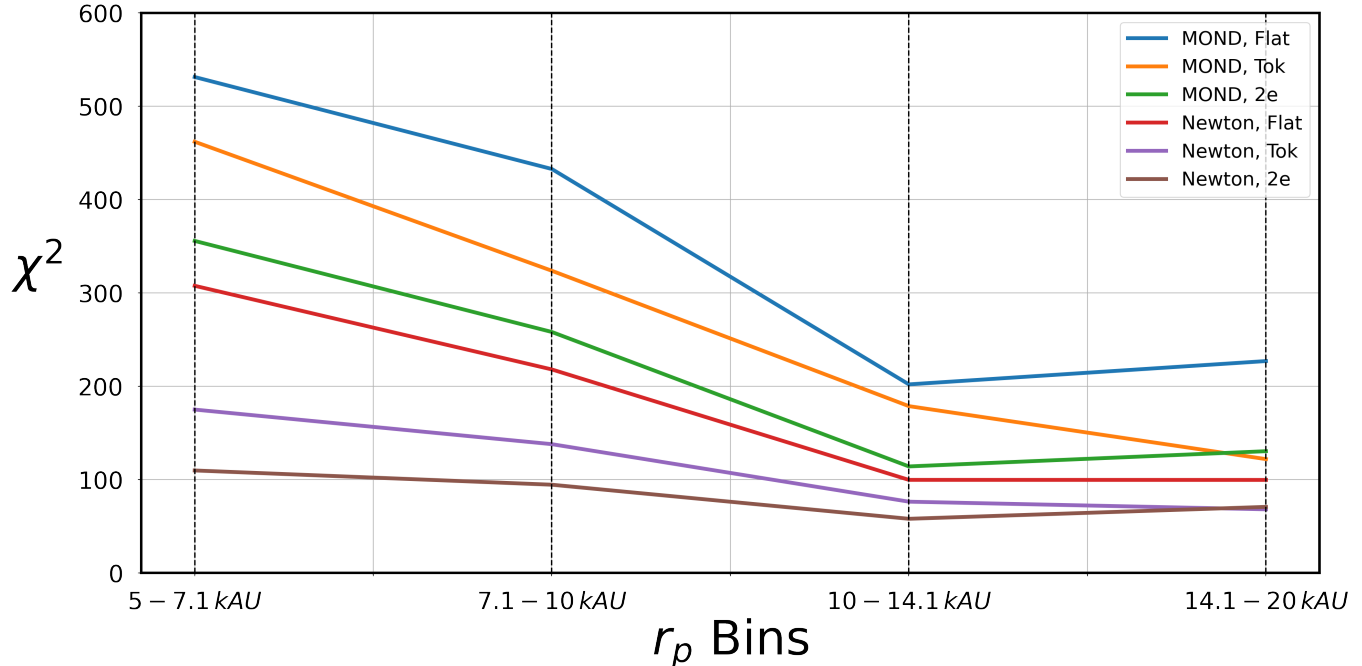


FIG. 16.— Plot comparing the χ^2 fitting results for each of the six orbit models (lines labelled in legend) against the four bins in projected separation bin r_p .

vergence to Newtonian gravity than we have modelled above, then the observable MOND shift will be correspondingly weaker.

3. One other concern from a referee was that the apparent-magnitude limit of our sample leads to a distance-dependent mass limit in our selected systems; to leading order this should cancel since the estimated masses are included in the definition of velocity ratio. To address this more directly, we constructed a volume-limited subsample by discarding binaries where either star has absolute magnitude $M_G > 9.61$, corresponding to apparent $G > 17$ at 300 pc; results for this volume-limited subsample are shown in Appendix B, and are qualitatively similar to the full sample.
4. Another possible issue is that of distance-dependent selection. We have explored cutting our above sample in halves at the median distance of 210 pc, and fitting separately to the closer and more distant halves of the sample. Results are shown in Appendix C; the closer half shows distinctly larger χ^2 differences, while the distant half shows less clear distinction between models; but the sense of the differences is similar between closer and distant halves.
5. As discussed above, a better understanding of the population of triples (and quadruples) is probably the key requirement to make the gravity test more secure. We could explore fitting with many variants of the triple model, but this is computationally expensive due to the many degrees of freedom, and may lead to degeneracies. The best route forward appears to be a followup observing programme to directly detect the additional object(s) in triple

systems. In a followup paper (Manchanda et al. 2022) we have simulated various followup methods: the results are positive in that overall some 80 – 95 percent of third objects are detectable by a combination of GAIA astrometric accelerations, deep seeing-limited imaging and followup speckle or coronagraphic imaging. Essentially all main-sequence companions are detectable by one or more methods, while undetectable objects are primarily cool brown dwarfs at separations $\gtrsim 25$ AU.

4.2. Comparison with Hernandez et al (2022) study

A recent paper by Hernandez et al. (2022), hereafter HCC22, has also studied wide binaries in GAIA DR3, and comes to a generally opposite conclusion that MOND is favoured over Newtonian gravity. This is mainly due to a levelling-off of the observed RMS velocity difference; their binaries at $r_p > 0.01$ pc or 2 kAU show a near-flat 1D rms velocity difference at a value near 0.5 km s^{-1} .

From the perspective of sample selection, the main difference to this work is that HCC22 use much more stringent constraints, e.g. $d < 130$ pc vs our 300 pc, RUWE < 1.2 instead of 1.4, and tight constraints on the colour-magnitude diagram; these tight cuts are mainly motivated by removing contamination from triple systems, clearly a desirable objective. However, the downside is that their surviving sample for final analysis is very much smaller: HCC22 Figure 7 shows < 200 binaries with $2.06 < r_p < 20.6$ kAU, compared to the 7276 used here between $5 < r_p < 20$ kAU. Due to their small sample, detailed histogram-fits are not practical and they use simple RMS velocity statistics; as is well known, RMS statistics are vulnerable to overestimation by a small fraction of contaminants at values many times larger than the pure-population RMS.

TABLE 4

NUMBER OF CANDIDATE BINARIES IN SELECTED RANGES OF PROJECTED SEPARATION AND VELOCITY RATIO: DATA, AND MODEL FITS FOR COMBINED BINARY (B), TRIPLES (T) AND FLYBYS (F) POPULATIONS, FOR NEWTONIAN GRAVITY AND FLAT ECCENTRICITY DISTRIBUTION. ROWS ARE RANGE OF PROJECTED SEPARATION, AS IN COLUMN 1. COLUMNS 2-4 ARE FOR ALL VELOCITY RATIOS, COLUMNS 5-7 FOR RATIOS < 1.4 , AND COLUMNS 8-10 FOR RATIOS BETWEEN 1.1 AND 1.4. RIGHTMOST COLUMN 11 IS THE χ^2 VALUE OF THE FIT.

r_p range	$v_p/v_C(r_p) < 7$				$v_p/v_C(r_p) < 1.4$				$1.1 < v_p/v_C(r_p) < 1.4$				χ^2
	Data	Fit(B)	Fit(T)	Fit(F)	Data	Fit(B)	Fit(T)	Fit(F)	Data	Fit(B)	Fit(T)	Fit(F)	
5 – 7.1 kAU	2510	1279.7	1279.7	71.9	2054	1279.7	762.4	36.6	226	107.4	174.3	7.6	307.7
7.1 – 10 kAU	1960	917.3	917.3	206.8	1489	917.3	514.9	95.6	186	65.5	118.2	20.4	218.0
10 – 14.1 kAU	1499	704.9	704.9	115.8	1116	704.9	374.4	44.8	165	50.4	86.7	10.5	99.7
14.1 – 20 kAU	1307	571.2	571.2	173.9	902	571.2	297.1	54.6	137	46.1	70.3	14.2	99.7

TABLE 5

SAME AS TABLE 4, BUT FOR MODEL ORBITS DRAWN FROM TOKOVININ ECCENTRICITY DISTRIBUTION.

r_p range	$v_p/v_C(r_p) < 7$				$v_p/v_C(r_p) < 1.4$				$1.1 < v_p/v_C(r_p) < 1.4$				χ^2
	Data	Fit(B)	Fit(T)	Fit(F)	Data	Fit(B)	Fit(T)	Fit(F)	Data	Fit(B)	Fit(T)	Fit(F)	
5 – 7.1 kAU	2510	1281.7	1281.7	0.0	2054	1281.7	772.5	0.0	226	78.6	168.4	0.0	175.0
7.1 – 10 kAU	1960	919.2	919.2	162.1	1489	919.2	520.8	74.9	186	71.6	116.7	16.0	138.0
10 – 14.1 kAU	1499	692.2	692.2	129.4	1116	692.2	372.5	50.1	165	56.1	84.5	11.7	76.4
14.1 – 20 kAU	1307	559.9	559.9	181.8	902	559.9	298.4	57.0	137	43.2	68.4	14.8	68.2

TABLE 6

SAME AS TABLE 4, BUT MODEL ORBITS DRAWN FROM $2e$ ECCENTRICITY DISTRIBUTION.

r_p range	$v_p/v_C(r_p) < 7$				$v_p/v_C(r_p) < 1.4$				$1.1 < v_p/v_C(r_p) < 1.4$				χ^2
	Data	Fit(B)	Fit(T)	Fit(F)	Data	Fit(B)	Fit(T)	Fit(F)	Data	Fit(B)	Fit(T)	Fit(F)	
5 – 7.1 kAU	2510	1264.9	1264.9	0.0	2054	1264.9	776.3	0.0	226	99.9	165.4	0.0	109.8
7.1 – 10 kAU	1960	911.0	911.0	156.3	1489	911.0	530.9	72.2	186	65.4	115.2	15.4	94.6
10 – 14.1 kAU	1499	689.3	689.3	125.0	1116	689.3	380.1	48.4	165	56.3	84.5	11.3	58.0
14.1 – 20 kAU	1307	552.7	552.7	197.2	902	552.7	298.6	61.9	137	38.8	65.9	16.1	70.8

In particular, the cuts used by HCC22 will likely not reject triples if the inner-orbit period is substantially longer than the 2.75 year DR3 timespan (when the deviation from linear motion is too small to boost the RUWE value), and inner angular separation is below ~ 0.5 arcsec; this leaves inner orbits from $\sim 5 - 50$ AU largely surviving their cuts, along with very faint third stars beyond 50 AU. Such systems can cause a large boost on the observed v_p of the wide system, as shown in simulations by [Manchanda et al. \(2022\)](#).

We note that there exist a handful of points in the upper-right corner of HCC22 Figure 7 which have 1D relative velocity differences $> 5\times$ higher than their Newtonian rms (blue line). In our Newtonian orbit models, pure-binary systems have a maximum 2D velocity difference approximately $2.4\times$ the population RMS at the same r_p ; in 1D the maximum is unchanged but the population RMS is $1/\sqrt{2}$ smaller, so this limit becomes $3.4\times$; MOND with external field effect can boost this to near $4\times$, but our simulations suggest that systems above $5\times$ the 1D rms are very unlikely to be pure binaries, and suggestive of residual triples.

As a check, we have investigated RMS and median statistics of our sample over the range $2 < r_p < 20$ kAU where the MOND effect is claimed by HCC22. Results are shown in Fig 17. Results are shown for several cuts on \tilde{v} from 5 down to 1.5 to reject contaminants. For the RMS values, there is a slow decline for $\tilde{v} < 5$ but a decline close to $r_p^{-0.5}$ for the smaller \tilde{v} cuts which reject the tail. The median statistic is more robust against

contaminants, and all samples show a decline close to $r_p^{-0.5}$. While our sample selection is different, this suggests that population RMS velocity differences without a \tilde{v} upper limit are strongly inflated by the tail of systems at $\tilde{v} > 2$ which cannot realistically be pure binaries. (If the MOND effect were so large as to allow pure binaries at $\tilde{v} > 2$, then the population mode (peak in our \tilde{v} histograms) would show an obvious shift rightwards with r_p , but such a shift is not seen).

We conclude that triple-system contamination boosting the RMS velocity differences can plausibly account for the MOND detection claimed by HCC22.

TABLE 7

AS TABLE 4, BUT FOR REALISTIC MOND GRAVITY MODEL AND ALL ORBITS DRAWN FROM A FLAT ECCENTRICITY DISTRIBUTION. TABLE SHOWS NUMBER OF CANDIDATE BINARIES IN SELECTED RANGES OF PROJECTED SEPARATION AND VELOCITY RATIO: DATA, AND MODEL FITS FOR BINARY(B), TRIPLES (T) AND FLYBYS (F) POPULATIONS. ROWS ARE RANGE OF PROJECTED SEPARATION, AS IN COLUMN 1. COLUMNS 2-4 ARE FOR ALL VELOCITY RATIOS, COLUMNS 5-7 FOR RATIOS < 1.4 , AND COLUMNS 8-10 FOR RATIOS BETWEEN 1.1 AND 1.4.

r_p range	$v_p/v_C(r_p) < 7$				$v_p/v_C(r_p) < 1.4$			$1.1 < v_p/v_C(r_p) < 1.4$				χ^2	
	Data	Fit(B)	Fit(T)	Fit(F)	Data	Fit(B)	Fit(T)	Fit(F)	Data	Fit(B)	Fit(T)		Fit(F)
5 – 7.1 kAU	2510	1223.6	1223.6	296.1	2054	1201.6	702.0	150.7	226	241.3	179.8	31.4	531.3
7.1 – 10 kAU	1960	907.8	907.8	334.2	1489	885.6	486.5	154.4	186	196.8	131.9	32.9	432.8
10 – 14.1 kAU	1499	744.0	744.0	87.2	1116	733.0	375.7	33.8	165	154.3	105.0	7.9	202.0
14.1 – 20 kAU	1307	620.4	620.4	137.1	902	614.5	303.4	43.0	137	146.5	86.0	11.2	227.0

TABLE 8

SAME AS TABLE 7, WITH REALISTIC MOND GRAVITY MODEL, BUT MODEL ORBITS DRAWN FROM TOKOVININ ECCENTRICITY DISTRIBUTION.

r_p range	$v_p/v_C(r_p) < 7$				$v_p/v_C(r_p) < 1.4$			$1.1 < v_p/v_C(r_p) < 1.4$				χ^2	
	Data	Fit(B)	Fit(T)	Fit(F)	Data	Fit(B)	Fit(T)	Fit(F)	Data	Fit(B)	Fit(T)		Fit(F)
5 – 7.1 kAU	2510	1318.3	1318.3	70.8	2054	1299.2	772.9	36.1	226	313.2	190.6	7.5	462.0
7.1 – 10 kAU	1960	937.1	937.1	219.2	1489	914.2	510.3	101.3	186	188.1	132.1	21.6	323.8
10 – 14.1 kAU	1499	738.9	738.9	86.2	1116	719.7	378.4	33.4	165	135.7	100.1	7.8	178.7
14.1 – 20 kAU	1307	600.2	600.2	126.9	902	588.1	300.4	39.8	137	101.1	80.9	10.4	122.0

TABLE 9

SAME AS TABLE 7 WITH MOND GRAVITY MODEL, BUT MODEL ORBITS DRAWN FROM $f(e) = 2e$ ECCENTRICITY DISTRIBUTION.

r_p range	$v_p/v_C(r_p) < 7$				$v_p/v_C(r_p) < 1.4$			$1.1 < v_p/v_C(r_p) < 1.4$				χ^2	
	Data	Fit(B)	Fit(T)	Fit(F)	Data	Fit(B)	Fit(T)	Fit(F)	Data	Fit(B)	Fit(T)		Fit(F)
5 – 7.1 kAU	2510	1325.5	1325.5	0.0	2054	1286.8	791.0	0.0	226	248.0	193.7	0.0	355.8
7.1 – 10 kAU	1960	953.6	953.6	154.8	1489	922.2	530.8	71.5	186	180.9	132.2	15.2	258.2
10 – 14.1 kAU	1499	731.1	731.1	69.5	1116	713.1	381.7	26.9	165	129.1	98.2	6.3	114.1
14.1 – 20 kAU	1307	589.0	589.0	151.0	902	576.4	300.6	47.4	137	97.6	78.3	12.3	130.5

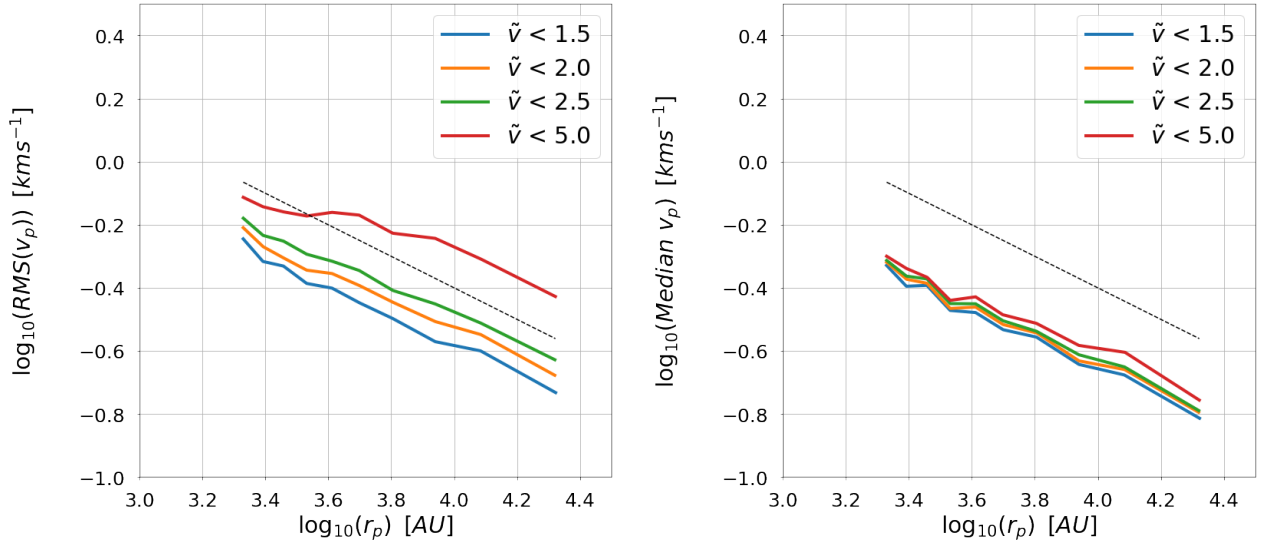


FIG. 17.— **Left panel:** The RMS sky-projected velocity difference vs r_p ; the sample of candidate binaries with $2 < r_p < 20$ kAU is divided into 10 r_p bins of near-equal numbers; a threshold of $\tilde{v} < 5, 2.5, 2$ or 1.5 is applied (see legend), then the RMS in each bin is shown. The dotted line indicates slope of -0.5 , with arbitrary zero-point for visibility. **Right panel:** Same as left panel, but showing the median sky-projected v_p instead of the RMS.

5. CONCLUSIONS

Following on from previous modelling work in PS18, and our observational study from GAIA DR2 in PS19, we have selected a new sample of candidate wide binaries from the recent GAIA Early Data Release 3 (EDR3); our cleaned sample contains 73,159 candidate binaries with distance ≤ 300 pc, projected separation ≤ 50 kAU and projected velocity difference ≤ 3 km s⁻¹. Comparisons with our previous PS19 sample and the independent binary sample of El-Badry et al (2021) show generally good consistency, after allowing for the different selection criteria used by El-Badry et al. We then estimate masses for each component using a main-sequence mass/luminosity relation, and our key observable is the projected velocity difference in each binary, from the GAIA proper motions assuming a common distance, divided by the velocity for a circular orbit at the observed projected separation; the statistics of this ratio can be reliably predicted from simulations, assuming random inclinations and orbital phases, given an assumed eccentricity distribution.

We have then focused on the subset of 9063 candidate wide binaries with projected separations between 5 kAU to 20 kAU, the most promising range for testing modified gravity; applying a *ruwe* cut reduces the sample to 7276 candidates. In agreement with PS19, the distributions show a clear “hump plus tail” shape, with a hump consistent with pure binaries and a tail to much larger velocity ratios. Dividing the range into four separation bins, we then fit each observed distribution as an arbitrary mixture of binary plus triple populations; we repeat the fitting for Newtonian gravity and one specific MOND model, and three assumed $f(e)$ eccentricity distributions. The fitting results show a clear preference for Newtonian gravity over MOND, with a high formal significance; this is largely because the MOND model fits overshoot the observed number of systems in the range $1.0 \leq \tilde{v} \leq 1.5$. Varying the model eccentricity distributions has little effect on this preference for standard gravity. However, this conclusion is only tentative at present due to using a somewhat over-simplified maximally-random model for the triple population. Further studies are clearly needed with a larger variety of models for the triple and flyby populations.

The prospects for future development of this test seem to be very good: GAIA EDR3 used only the first 33 months of GAIA survey data, while there are 7.5 years existing at present, and projected GAIA operations extend to 10 years, so the precision will substantially improve and allow even larger samples in future. This will be helpful, but the statistical uncertainties seem to be already sub-dominant now; the major uncertainty at present appears to be in the modelling and fitting of the presumed triple and flyby population contributing the tail of high-velocity systems.

There are interesting prospects for observationally detecting or constraining the triples, including for example: searches for faint companions in deep sky surveys; adaptive-optics or speckle imaging to directly resolve inner binaries in triples; searches for astrometric accelerations or excess residuals with future GAIA data; and high-precision radial velocities from ground-based data, including possible time-dependence. In a followup study (Manchanda et al. 2022) we have explored detection

prospects for our simulated triples, with very promising conclusions: a high percentage of triples should be directly detectable as such. Such programs may require substantial amounts of telescope time to build up good statistics of triples and other contaminants, but has a potentially large payoff in a decisive test of acceleration-based modified gravity models similar to MOND.

ACKNOWLEDGEMENTS

We thank two anonymous referees for comments which significantly improved the paper. We thank Indranil Banik for many helpful discussions, and Zizhen Lin for contributions to the triple-system simulations. CP has been supported by Colin Lee, Gary Barr, and Adel Szabo Malcolm (Legal & General Investment Management), Peter Jackson (Outra) and Konstantin Orfenov (BNP Paribas).

DATA AVAILABILITY

The original data used in this paper is publicly available. The Gaia data can be retrieved through the Gaia archive (<https://gea.esac.esa.int/archive>). The binary catalogue CWB-EDR3 will be made available on <https://zenodo.org> on acceptance of this paper.

REFERENCES

- Akerib, D. S., Alsum, S., Araújo, H. M., et al. 2016, ArXiv e-prints, Arxiv [1608.07648]
- Arenou, F., Luri, X., Babusiaux, C., et al. 2018, *A&A*, **616**, A17
- Banik, I. & Zhao, H. 2018, *MNRAS*, **480**, 2660
- Barrientos, E., Lobo, F. S. N., Mendoza, S., Olmo, G. J., & Rubiera-Garcia, D. 2018, *Phys. Rev. D*, **97**, 104041
- Bekenstein, J. D. 2004, *Phys. Rev. D*, **70**, 083509
- Bullock, J. S. & Boylan-Kolchin, M. 2017, *ARA&A*, **55**, 343
- Clarke, C. J. 2020, *MNRAS*, **491**, L72
- Close, L. M., Richer, H. B., & Crabtree, D. R. 1990, *AJ*, **100**, 1968
- Coronado, J., Sepúlveda, M. P., Gould, A., & Chanamé, J. 2018, *MNRAS*, **480**, 4302
- Dhital, S., West, A. A., Stassun, K. G., & Law, N. M. 2013, *Astronomische Nachrichten*, **334**, 14
- El-Badry, K. & Rix, H.-W. 2018, *MNRAS*, **480**, 4884
- El-Badry, K., Rix, H.-W., & Heintz, T. M. 2021, *MNRAS*, **506**, 2269
- Famaey, B. & McGaugh, S. S. 2012, *Living Rev. Relativ.*, **15**, 10
- Gaia Collaboration. 2016, *A&A*, **595**, A1
- Gaia Collaboration. 2020a, arXiv e-prints, arXiv:2012.01533
- Gaia Collaboration. 2020b, arXiv e-prints, arXiv:2012.02061
- Hernandez, X. 2019, ArXiv e-prints, Arxiv [1901.10605v2]
- Hernandez, X., Cookson, S., & Cortés, R. A. M. 2022, *MNRAS*, **509**, 2304
- Hernandez, X., Jiménez, A., & Allen, C. 2014, in *Accelerated Cosmic Expansion*, Vol. 38, 43
- Hernandez, X., Jiménez, M. A., & Allen, C. 2012a, in *Journal of Physics Conference Series*, Vol. 405, *Journal of Physics Conference Series*, 012018
- Hernandez, X., Jiménez, M. A., & Allen, C. 2012b, *EPJC*, **72**, 1884
- Hwang, H.-C., Ting, Y.-S., & Zakamska, N. L. 2022, *MNRAS* [2111.01789]
- Jiang, Y.-F. & Tremaine, S. 2010, *MNRAS*, **401**, 977
- Kouwenhoven, M. B. N., Goodwin, S. P., Parker, R. J., et al. 2010, *MNRAS*, **404**, 1835
- Kroupa, P. 2015, *Canadian Journal of Physics*, **93**, 169
- Lépine, S. & Bongiorno, B. 2007, *AJ*, **133**, 889
- Manchanda, D., Sutherland, W., & Pittordis, C. 2022, arXiv e-prints, arXiv:2210.07781
- Matvienko, A. S. & Orlov, V. V. 2015, *Astronomy Letters*, **41**, 824
- McGaugh, S., Lelli, F., & Schombert, J. 2016, *Phys. Rev. Lett.*, **117**, 201101
- McGaugh, S. S. 2016, *ApJL*, **832**, L8
- Milgrom, M. 1983, *ApJ*, **270**, 365
- Oh, S., Price-Whelan, A. M., Hogg, D. W., Morton, T. D., & Spergel, D. N. 2017, *AJ*, **153**, 257
- Pawlowski, M. S., Famaey, B., Jerjen, H., et al. 2014, *MNRAS*, **442**, 2362
- Pecaut, M. J. & Mamajek, E. E. 2013, *ApJS*, **208**, 9
- Pittordis, C. & Sutherland, W. 2018, *MNRAS*, **480**, 1778
- Pittordis, C. & Sutherland, W. 2019, *MNRAS*, **488**, 4740
- Planck Collaboration XIII. 2016, *A&A*, **594**, A13
- Riello, M., De Angeli, F., Evans, D. W., et al. 2021, *A&A*, **649**, A3
- Scarpa, R., Ottolina, R., Falomo, R., & Treves, A. 2017, *International Journal of Modern Physics D*, **26**, 1750067
- Shaya, E. J. & Olling, R. P. 2011, *ApJS*, **192**, 2
- Tokovinin, A. 2020, *MNRAS*, **496**, 987
- Tokovinin, A. & Kiyaveva, O. 2016, *MNRAS*, **456**, 2070
- Weinberg, M. D., Shapiro, S. L., & Wasserman, I. 1987, *ApJ*, **312**, 367
- Yoo, J., Chanamé, J., & Gould, A. 2004, *ApJ*, **601**, 311

APPENDIX

COMPARISON WITH PS19 SAMPLE FROM DR2

Here we compare our new EDR3 sample with the wide binary sample from PS19, where very similar methods were used to find candidates. The CWB-DR2 sample of 24,282 candidates is compared via matching on RA & Dec with 1'' search radius with the current WB-EDR3 sample of size 92,677 (before any cuts applied). In an ideal case all would have been recovered, since our distance and magnitude limits are expanded compared to PS19. We found that of the 24,282 binaries in the cleaned sample of PS19, 1696 or $\approx 7\%$ did not match a binary in WB-EDR3, before cleaning. This 7 percent of non-matches appears rather larger than expected, so we investigated the causes of these non-matched DR2 binary candidates.

On matching the individual stars, we found that 159 of the 1696 “missing” binaries had one or both stars not matching an EDR3 single star within a 1'' radius, presumably due to deblending or other reasons; since these are only 0.65 percent of the original CWB-DR2, we have not followed up this small minority. For the other 1537 pairs where both DR2 stars matched an EDR3 star, but the DR2 binary did not appear in WB-EDR3, we re-ran a binary search with the only selection criterion as $r_p < 50$ kAU, resulting in 1518 binaries recovered, with binary parameters such as v_p , r_p and parallax differences re-calculated from the EDR3 data.

We then investigated which of the cut(s) were failed for each of these 1518 pairs. After applying star-quality cuts in EDR3 (using the same method as described in section 2.5), 307 failed for one or both stars, while 1211 binaries survived. We then found that the most common reason for failure was the criterion $|d_1 - d_2| \leq 4\sigma_{\Delta d}$; this resulted in 1153 failures (1,008 after applying star-quality cuts), as shown in Figure 18. The second most common reason was $v_p < 3 \text{ km s}^{-1}$, which accounted for another 190 (183 after applying star-quality cuts) binaries exceeding the cut given the EDR3 values. Table 10 shows the number of Passed & Failed for each of the criteria.

From that Table, it is clear that the main reason for non-recovery of PS19 binaries is pairs with parallax differences below our threshold in DR2, but above threshold in EDR3. Our 4σ threshold is fairly generous, so this is rather unexpected for Gaussian errors. This might perhaps be explained by a population of hierarchical triples for which orbital motion results in substantially non-Gaussian parallax errors in the standard 5-parameter fits. Future data from DR4 or beyond may help to clarify this; for the present, we do not use these “missing” binaries in the rest of this paper.

Additionally, in Figs. 19 to 21 we show comparisons of velocity errors, distances and masses between PS19 and the new sample here, showing results as expected.

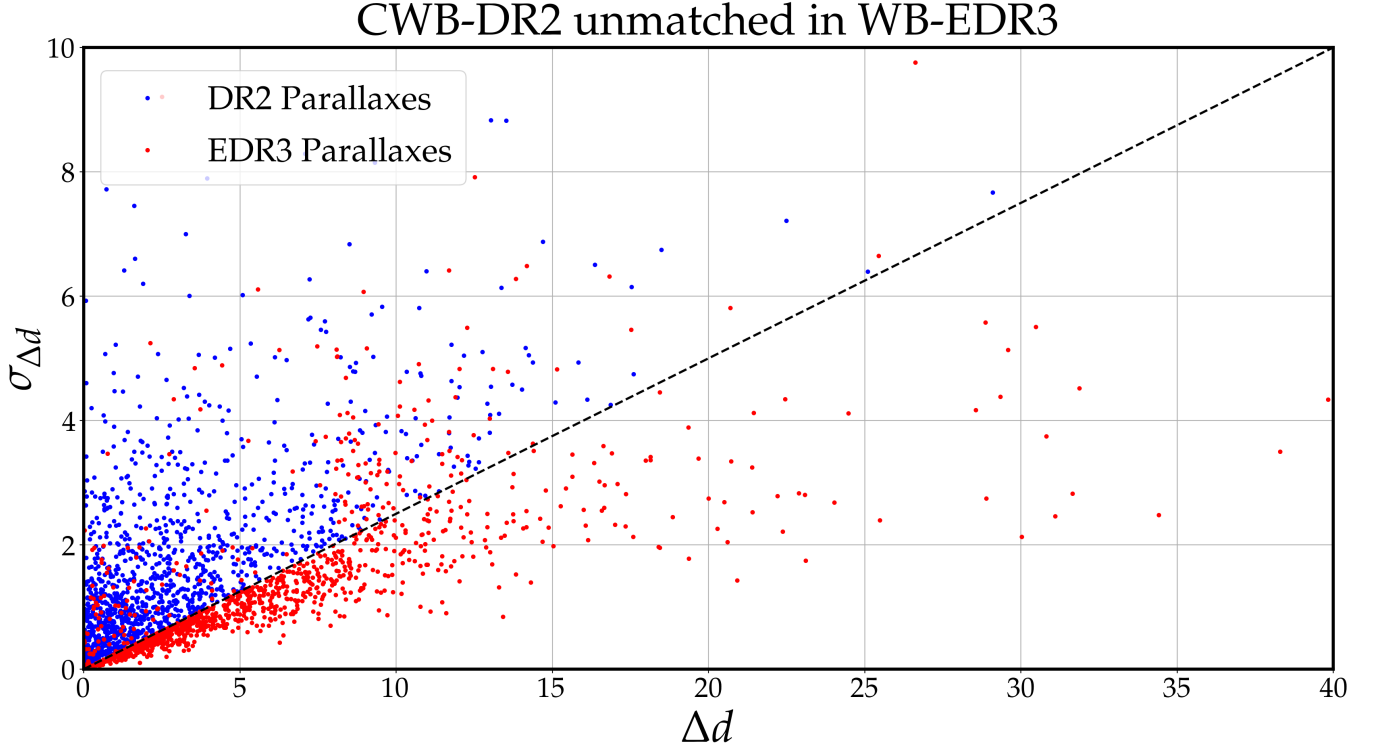


FIG. 18.— Scatter plot for candidate binaries present in previous CWB-DR2 sample, but absent from WB-EDR3. The plot shows uncertainty in the difference in parallax distances $\sigma_{\Delta d}$ vs difference in distances Δd . The blue points show the values from CWB-DR2, while red points show updated values for the same systems from EDR3 data. The sloping line is our selection criterion on this ratio. This plot shows that the most common reason for non-recovered DR2 binary candidates is those with larger Δd in DR3.

TABLE 10
REASONS FOR SUBSAMPLE OF PS19 BINARIES NOT RECOVERED IN CURRENT CWB-EDR3 SAMPLE: NUMBER OF PASSED/FAILED FOR EACH CRITERION OF THE CANDIDATE BINARIES. VALUES IN BRACKETS ARE WITHOUT STAR-QUALITY CUTS.

Criterion	Passed	Failed
$r_p < 50 \text{ kAU}$	1,211 (1,518)	0
$ d_1 - d_2 < 8 \text{ pc}$	880 (978)	331 (540)
$ d_1 - d_2 \leq 4\sigma_d$	203 (365)	1,008 (1,153)
$\Delta v_p < 3 \text{ km s}^{-1}$	1,073 (1,328)	138 (190)
Combination of all criteria above	0	1,211 (1,518)

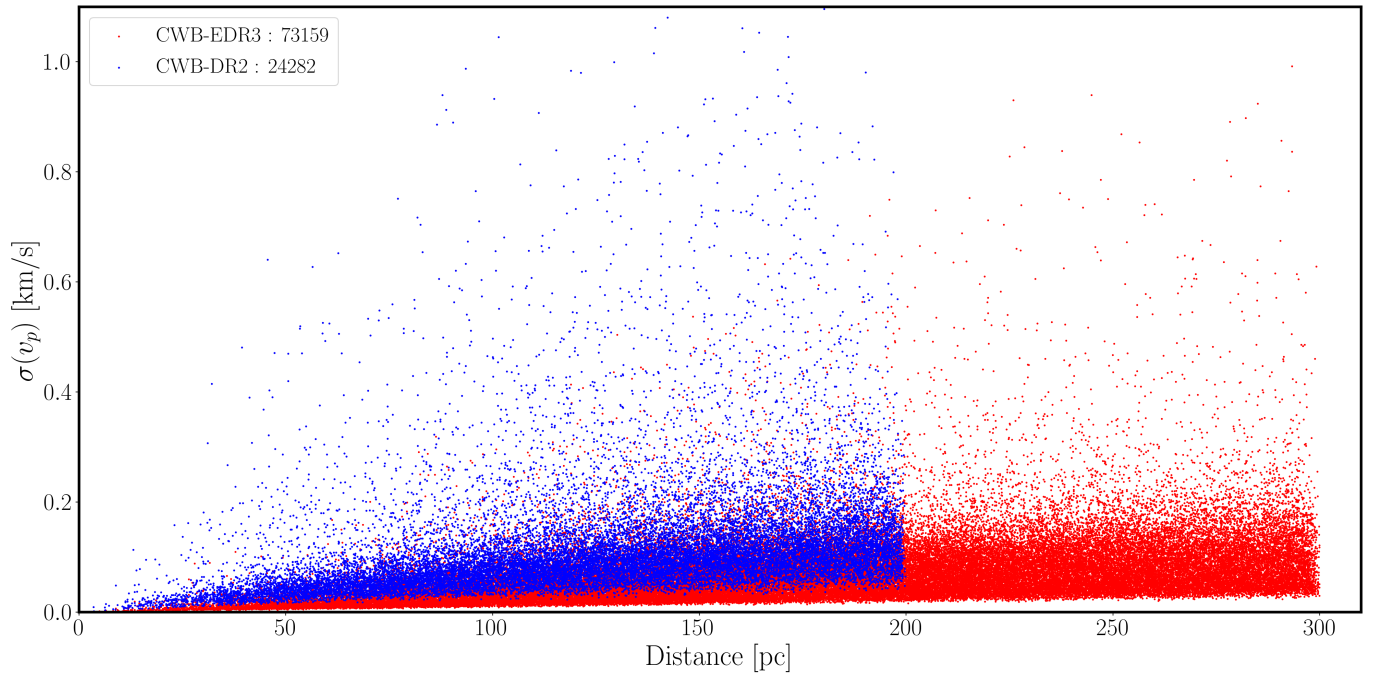


FIG. 19.— Scatter plot of rms velocity uncertainty $\sigma(v_p)$ versus mean distance for CWB-EDR3 (red) and CWB-DR2 (blue) binaries surviving all cuts.

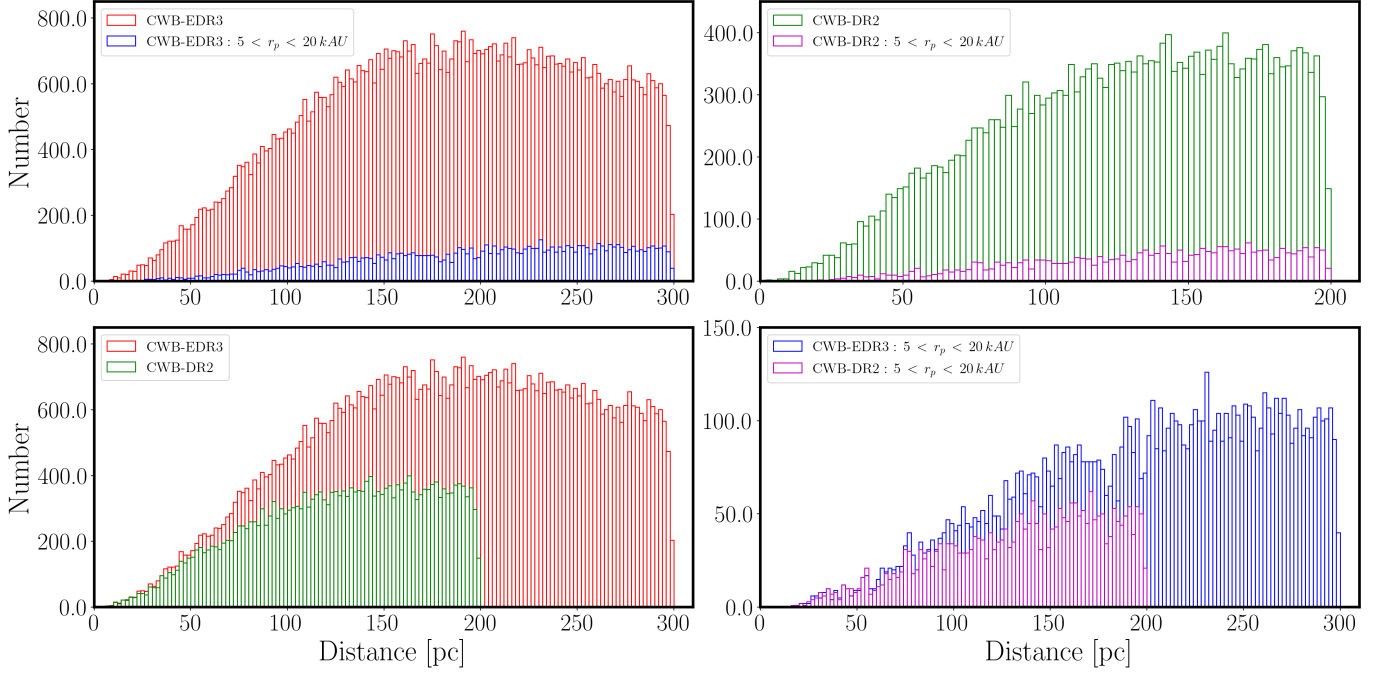


FIG. 20.— Histograms of average distance for the candidate binaries. (Top Right) histogram shows all 73,159 CWB-EDR3, also showing the subset with $5 < r_p < 20 \text{ kAU}$ comparing between EDR3 and GDR2. (Top Left) same as the (Top Right) histogram but for CWB-DR2. (Bottom Left) compares between CWB-EDR3 and CWB-DR2, and same for the (Bottom Right) but for the subset of $5 < r_p < 20 \text{ kAU}$.

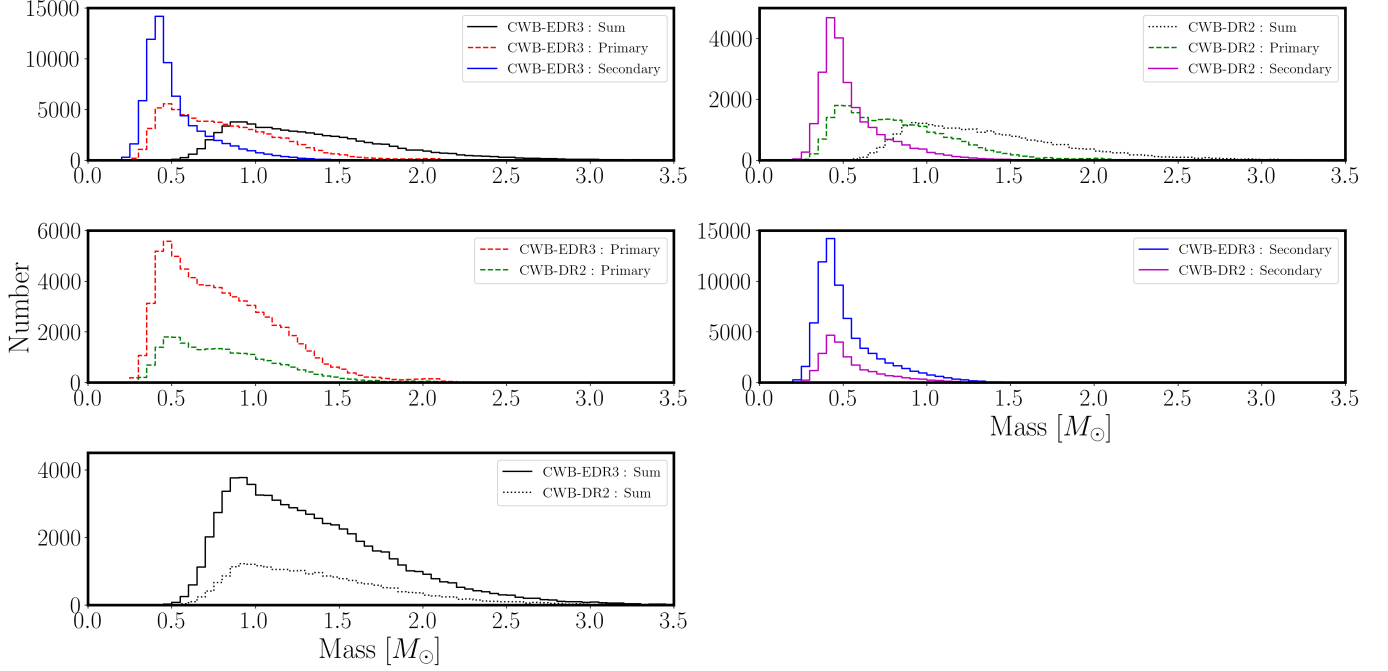


FIG. 21.— Histograms of estimated masses for the candidate binaries. For the CWB-EDR3 sample, the black solid line shows combined system mass; dashed red line shows the primary (more massive) star, and blue line shows the secondary star. For the CWB-DR2 sample, the dashed black line shows combined system mass; dashed green line shows the primary (more massive) star, and magenta line shows the secondary star. The rest of the histograms compared the combined system mass, primary and secondary mass between CWB-EDR3 and CWB-DR2.

VOLUME LIMITED SUBSAMPLE

A concern was raised by a referee that the $G < 17$ apparent magnitude limit leads to a distance-dependent selection, i.e. loss of low-mass systems at larger distance; to leading order we would not expect any effect since the system masses are scaled out in the velocity ratio \tilde{v} . To test for any effect, we applied a volume-limit to our CWB-EDR3 sample, by discarding all binaries where either star would be fainter than $G > 17$ if at 300 pc, which corresponds to a Gaia absolute magnitude cut $M_G < 9.61$. This reduces the sample from 77,159 to 44,285 candidate binaries, hereafter labelled as CWB-EDR3-VolLim. We also repeated the fit procedure as described in Section 4, fitting the two gravity and three $f(e)$ models to the volume-limited subsample. The resulting χ^2 values are shown in 22, and follow essentially the same rank-ordering as the full sample. For brevity we only show histograms (see Figures 23 and 24), and tables (Tables 11 and 12) for both gravity models with the $f(e) = 2e$ eccentricity distribution, i.e. the best eccentricity model for both Newton and MOND.

For the volume-limited subsample, we note that the fit χ^2 values are marginally improved over the full subsample, as shown in Tables 11 and 12; though the χ^2 differences between Newtonian and MOND are reduced, as expected given the $0.67\times$ reduction in sample size hence relatively larger Poisson errors.

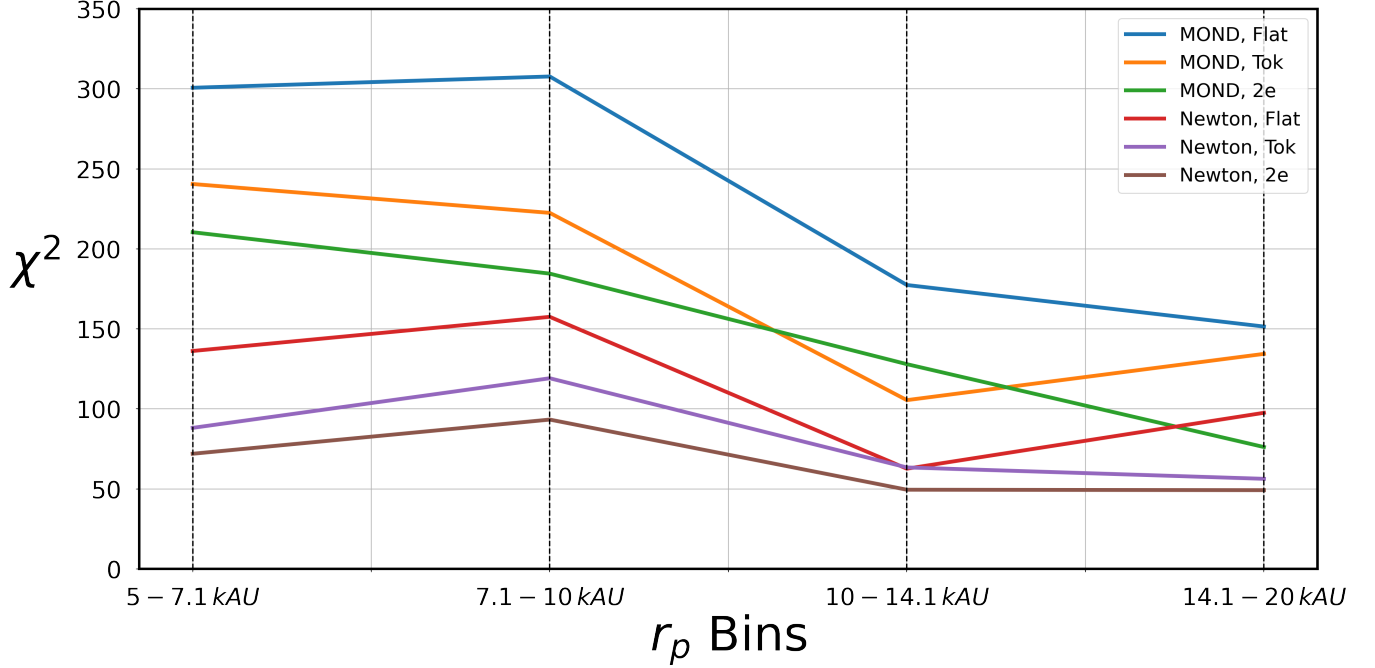


FIG. 22.— Same as Figure 16, except with the Volume-limit cut applied, showing a plot comparing the χ^2 fitting results for each of the six orbit models (lines labelled in legend) against the four bins in projected separation bin r_p .

TABLE 11

NUMBER OF CANDIDATE BINARIES IN SELECTED RANGES OF PROJECTED SEPARATION AND VELOCITY RATIO: DATA, AND MODEL FITS FOR COMBINED BINARY (B) AND TRIPLES (T) POPULATIONS, FOR NEWTONIAN GRAVITY AND FLAT ECCENTRICITY DISTRIBUTION. ROWS ARE RANGE OF PROJECTED SEPARATION, AS IN COLUMN 1. COLUMNS 2-4 ARE FOR ALL VELOCITY RATIOS, COLUMNS 5-7 FOR RATIOS < 1.4 , AND COLUMNS 8-10 FOR RATIOS BETWEEN 1.1 AND 1.4. RIGHTMOST COLUMN 11 IS THE χ^2 VALUE OF THE FIT. SAME AS TABLE 4, BUT MODEL ORBITS DRAWN FROM $2e$ ECCENTRICITY DISTRIBUTION.

r_p range	$v_p/v_C(r_p) < 7$				$v_p/v_C(r_p) < 1.4$				$1.1 < v_p/v_C(r_p) < 1.4$				χ^2
	Data	Fit(B)	Fit(T)	Fit(F)	Data	Fit(B)	Fit(T)	Fit(F)	Data	Fit(B)	Fit(T)	Fit(F)	
5 - 7.1 kAU	1594	777.10	777.10	51.93	1268	777.10	476.89	26.43	148	63.07	101.61	5.51	72.00
7.1 - 10 kAU	1304	597.01	597.01	138.72	988	597.01	347.90	64.09	117	45.39	75.48	13.66	93.35
10 - 14.1 kAU	1007	460.08	460.08	97.35	746	460.08	253.69	37.70	109	38.23	56.40	8.82	49.52
14.1 - 20 kAU	874	355.58	355.58	163.28	592	355.58	192.13	51.23	96	32.23	42.43	13.34	49.25

TABLE 12

AS TABLE 4, BUT FOR REALISTIC MOND GRAVITY MODEL AND ALL ORBITS DRAWN FROM A FLAT ECCENTRICITY DISTRIBUTION. TABLE SHOWS NUMBER OF CANDIDATE BINARIES IN SELECTED RANGES OF PROJECTED SEPARATION AND VELOCITY RATIO: DATA, AND MODEL FITS FOR BINARY (B) AND TRIPLES (T) POPULATIONS. ROWS ARE RANGE OF PROJECTED SEPARATION, AS IN COLUMN 1. COLUMNS 2-4 ARE FOR ALL VELOCITY RATIOS, COLUMNS 5-7 FOR RATIOS < 1.4 , AND COLUMNS 8-10 FOR RATIOS BETWEEN 1.1 AND 1.4. SAME AS TABLE 7 WITH MOND GRAVITY MODEL, BUT MODEL ORBITS DRAWN FROM $f(e) = 2e$ ECCENTRICITY DISTRIBUTION.

r_p range	$v_p/v_C(r_p) < 7$				$v_p/v_C(r_p) < 1.4$				$1.1 < v_p/v_C(r_p) < 1.4$				χ^2
	Data	Fit(B)	Fit(T)	Fit(F)	Data	Fit(B)	Fit(T)	Fit(F)	Data	Fit(B)	Fit(T)	Fit(F)	
5 - 7.1 kAU	1594	808.26	808.26	59.43	1268	774.30	482.34	30.24	148	129.05	118.11	6.30	210.44
7.1 - 10 kAU	1304	625.55	625.55	129.04	988	612.44	348.16	59.62	117	104.88	86.69	12.71	184.57
10 - 14.1 kAU	1007	478.47	478.47	96.63	746	467.04	249.80	37.42	109	81.41	64.24	8.76	128.00
14.1 - 20 kAU	874	373.91	373.91	137.54	592	373.91	190.82	43.15	96	59.46	49.69	11.23	76.19

DISTANCE-CUT SUBSAMPLES

Here we investigate whether there is a systematic distance-dependent effect; we have cut the wide-binary sample in half at the median distance of 210 pc, then repeated the fit procedure from Section 4 separately for the near half ($d < 210$ pc) and the far half ($210 < d < 300$ pc) of the sample. The results for the χ^2 values are shown in Figure 25 for the near half, and Figure 26 for the distant half.

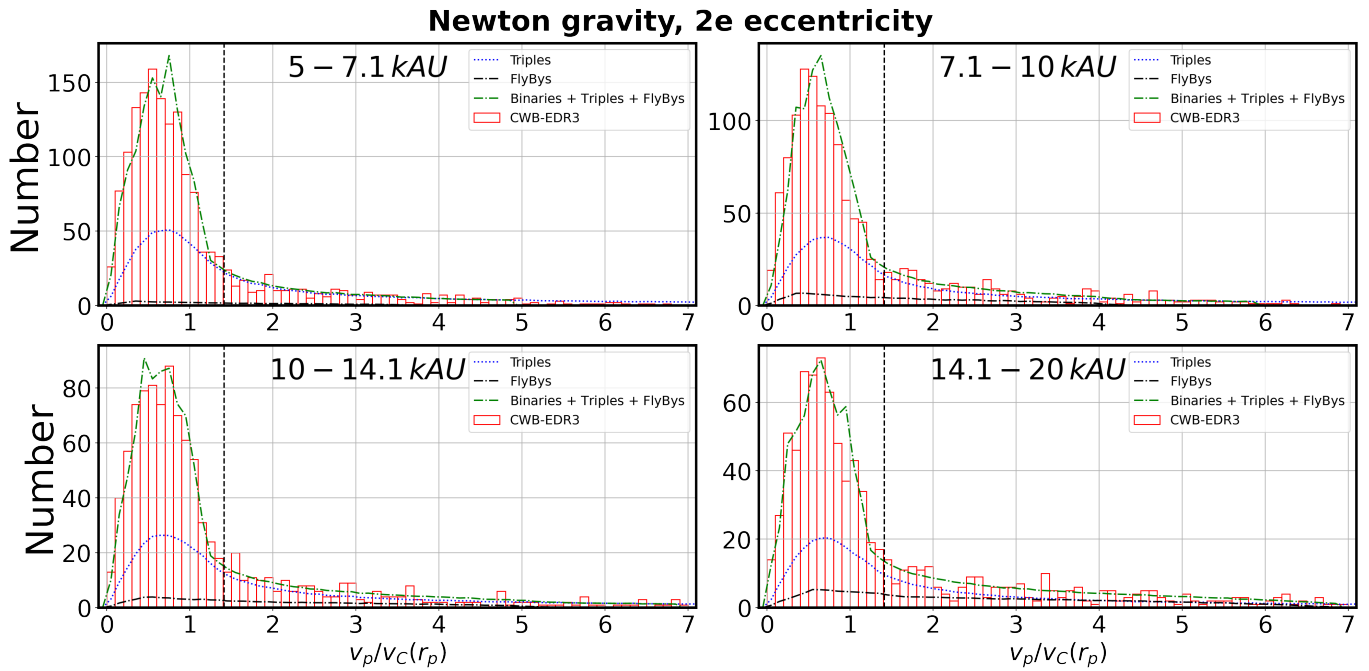


FIG. 23.— Same as Figure 12 with Newtonian gravity and $f(e) = 2e$ eccentricity distribution, except with the Volume-limit cut applied.

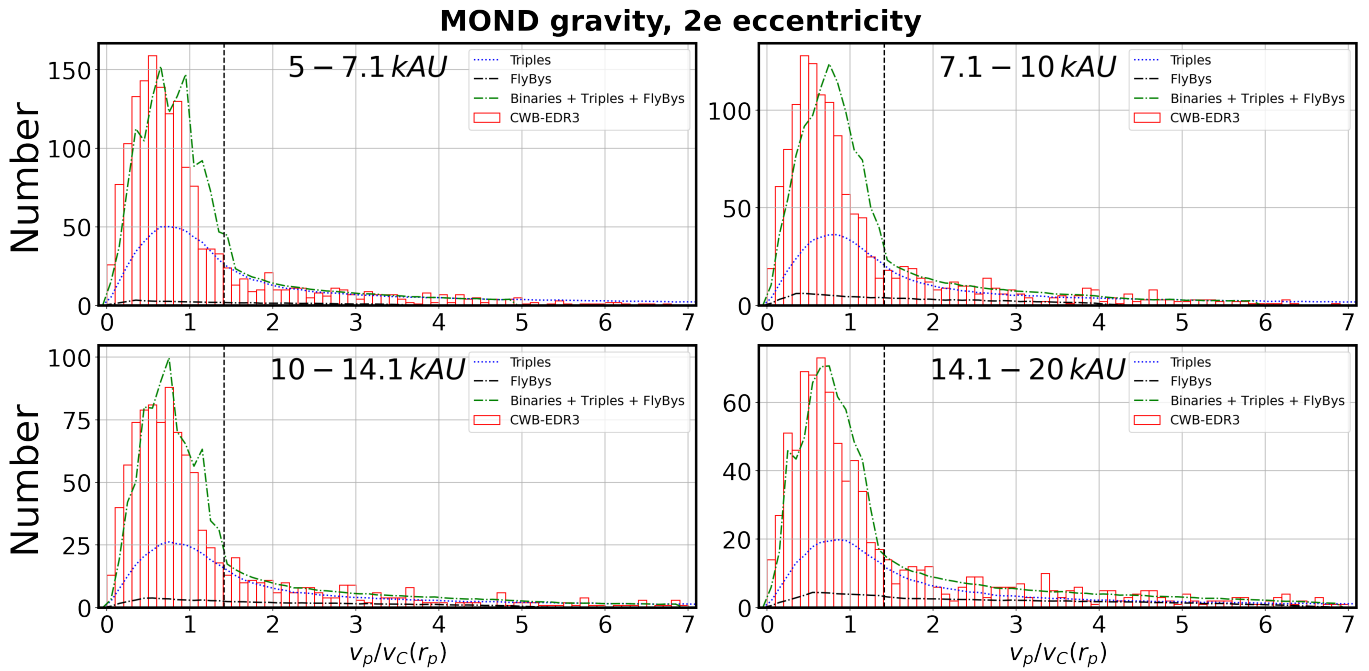


FIG. 24.— Same as Figure 15 with realistic MOND gravity model and $f(e) = 2e$ eccentricity distribution, except with the Volume-limit cut applied.

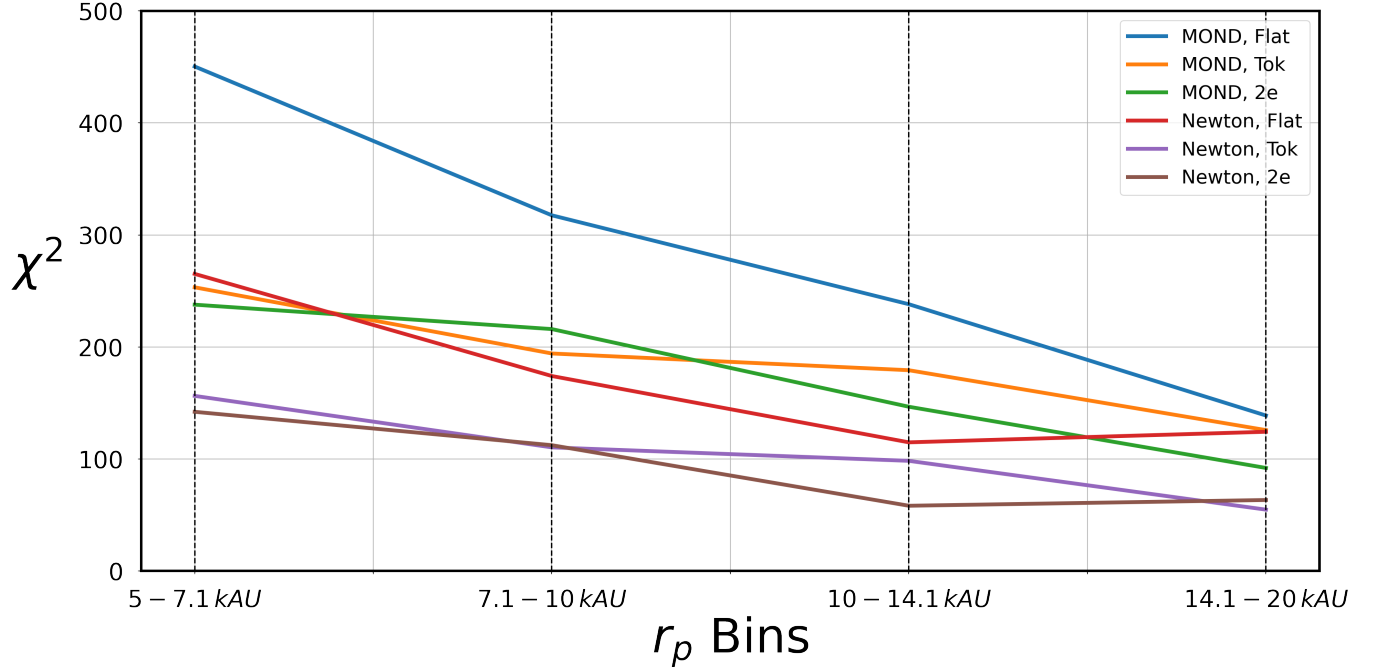


FIG. 25.— Same as Figure 16, for the near half of the sample at $d < 210$ pc; the plot compares the χ^2 fitting results for each of the six orbit models (lines labelled in legend) against the four bins in projected separation r_p .

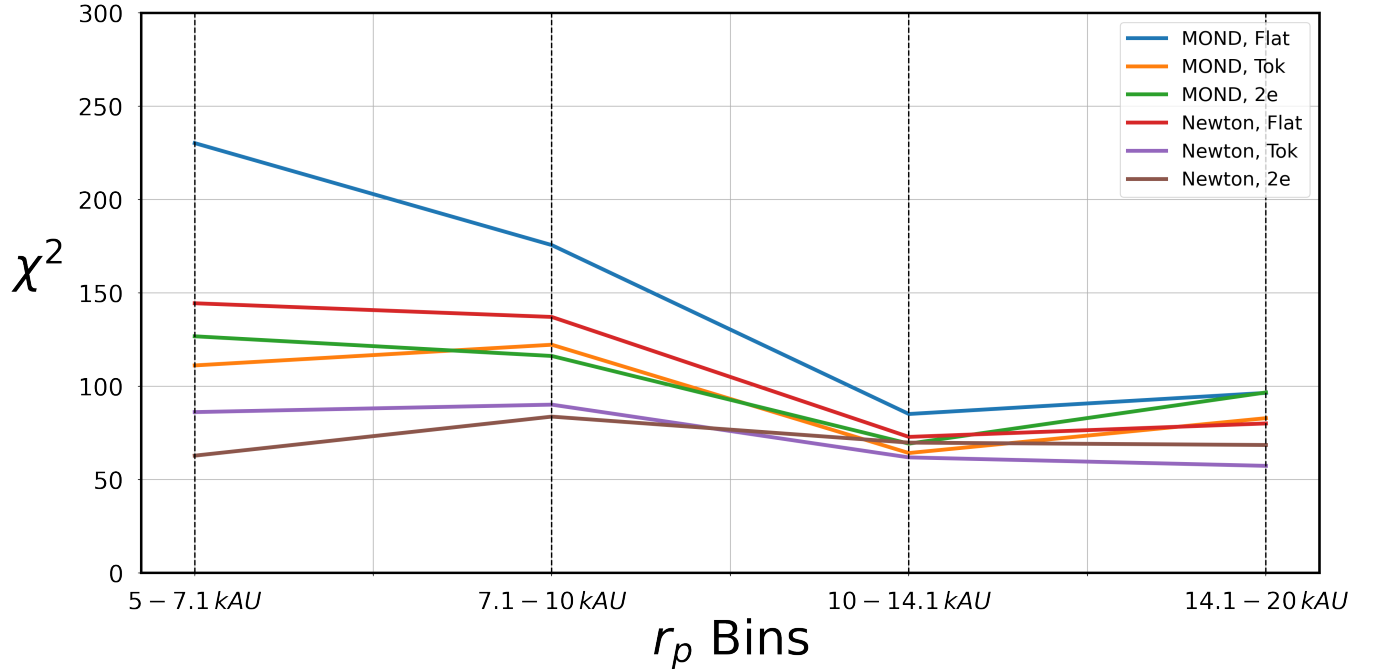


FIG. 26.— Same as Figure 16, for the far half of the sample at $210 \text{ pc} < d < 300$ pc; the plot compares the χ^2 fitting results for each of the six orbit models (lines labelled in legend) against the four bins in projected separation r_p .